

# PECan: A Canadian Parabolic Equation Model for Underwater Sound Propagation

Gary H. Brooke

*Integrated Performance Decisions*  
947 Fort Street, Victoria, BC, Canada V8V 3K3

David J. Thomson & Gordon R. Ebbeson

*Defence Research Establishment Atlantic*  
P.O. Box 1012, Dartmouth, NS Canada B2Y 3Z7

(March 28, 2000)

PECan is a **C**anadian  $N \times 2D/3D$  parabolic equation (**PE**) underwater sound propagation model that was developed for matched-field processing applications. It is based on standard square-root operator and/or propagator approximations that lead to an alternating direction solution of the 3D problem. A 2D split-step Padé approximation is employed for propagation in range. The 3D azimuthal corrections are computed using either a split-step Fourier method or a Crank-Nicolson finite-difference approximation. It features a heterogeneous formulation of the differential operators, an offset vertical grid, energy conservation, a choice of initial field including self-starter, and both absorbing and nonlocal boundary conditions. Losses due to shear wave conversion in an elastic bottom are handled in the context of a complex density approximation. In this paper, PECan is described and validated against some standard benchmark solutions to underwater acoustics problems. Subsequently, PECan is applied to several single-frequency test cases that were offered for numerical consideration at the SWAM'99 Shallow Water Acoustic Modelling workshop.

43.30Bp

## I. INTRODUCTION

Canada's three ocean environments encompass large continental shelf areas. Consequently, long range propagation of underwater sound is strongly influenced by interactions with the top and bottom ocean boundaries in these regions. At the ocean surface, this interaction typically involves a wind-driven sea surface or the rough underside of multi-year Arctic pack ice. Alternatively, at the ocean bottom, range-dependent bathymetry and small-scale roughness can significantly effect the propagation of acoustic energy. Since modern source localization schemes such as matched-field processing [1] rely on correlating acoustic predictions with measured array data, it is important to properly and efficiently model the coherent sound field in such environments.

PECan is a **C**anadian **P**arabolic **E**quation (PE) model that has been developed and enhanced in recent years to become a fully modern underwater acoustic propagation modelling tool capable of computing acoustic predictions in realistic oceanic environments. Numerical propagation models based on the parabolic approximation [2] have undergone extensive improvements in the past decade [3, pp. 343–412]. In particular, as attention has shifted to shallow water, finite-difference methods [4–6] have assumed a more prominent role. Current finite-difference algorithms are accurate [7–9], energy-conserving [10], and efficient [11]. Moreover, recent models are also capable of treating complicated waveguide effects such as elasticity [12–14], backscatter [15–17], porosity [18–20], and surface roughness [21–23]. PECan incorporates several of these extended capabilities into a versatile propagation model that generates coherent acoustic predictions in 3D range-dependent environments including elastic properties in the sediments. It features an energy-conserving, split-step Padé algorithm to march the acoustic field in range, depth, and azimuth, i.e.,  $N \times 2D$  propagation modelling. The user can optionally choose to correct the  $N \times 2D$  field using an azimuthal-coupling operator thereby providing an approximation to full 3D acoustic modelling.

As part of the 1999 Shallow Water Acoustics Modeling (SWAM'99) workshop [24], PECan (along with several other acoustic propagation models) was exercised against tonal benchmark-type test cases that included range-dependent oceanographic parameters and bathymetry, 3D effects, and shear in the ocean bottom. In this document, we present the relevant mathematical analysis underlying the current version of the PECan model. Specifically, we present the various operator approximations necessary to develop a propagation algorithm for the PE field in range, depth, and bearing. Also, we outline the analysis that is required to account for energy conservation [10], shear in the sediments [25], a self-starter [26], and nonlocal boundary conditions to represent the effects of a rough ocean surface [21–23] or a homogeneous ocean bottom [27–29]. Finally, we devote a brief discussion to the application of the PECan algorithm to selected tonal SWAM'99 test cases. We examine specific issues associated with (i) environmental

interpolation onto the PE computational grid, (ii) reciprocity in the context of PE algorithms, and (iii) 3D coupling induced by azimuthal bathymetric variations.

## II. PECAN THEORY

Consider a range-independent acoustic medium in cylindrical coordinates  $(r, z, \varphi)$ , bounded above by a free surface at  $z = 0$ , with a sound-speed profile that supports long range propagation (as  $r \rightarrow \infty$ ) in the upper part of the waveguide. For a harmonic point source located at  $(0, z_s, 0)$ , the spatial part of the pressure  $p(r, z, \varphi)e^{-i\omega t}$  in  $r > 0$  satisfies the scalar Helmholtz equation

$$r^{-1} \frac{\partial}{\partial r} \left( r \frac{\partial p}{\partial r} \right) + \rho \frac{\partial}{\partial z} \left( \rho^{-1} \frac{\partial p}{\partial z} \right) + r^{-2} \frac{\partial^2 p}{\partial \varphi^2} + k_0^2 N^2 p = 0. \quad (1)$$

Here,  $k_0 = \omega/c_0$  is a reference wavenumber,  $\rho(z)$  is the density,  $N(z) = n(z)[1 + i\alpha(z)]$  where  $n(z) = c_0/c(z)$  is the refractive index,  $c(z)$  is the sound speed, and  $\alpha(z)$  is the absorption loss. For numerical work, it is convenient to introduce the reduced 3D-field  $\Psi$  via

$$p(r, z, \varphi) = \frac{\exp ik_0 r}{\sqrt{r}} \Psi(r, z, \varphi). \quad (2)$$

Substituting Eq. (2) into Eq. (1) and factoring the result into outgoing and incoming fields yields the one-way, far-field ( $k_0 r \gg 1$ ) wave equation for the forward-propagating component in the form

$$\frac{\partial \Psi}{\partial r} = ik_0 \left( -1 + \sqrt{1 + X_3} \right) \Psi. \quad (3)$$

In Eq. (3),  $X_3$  denotes the 3D differential operator

$$X_3 = X_2 + X_\varphi, \quad (4)$$

where  $X_2$  is the 2D depth operator in the  $rz$ -plane

$$X_2 = N^2 - 1 + k_0^{-2} \rho \frac{\partial}{\partial z} \left( \rho^{-1} \frac{\partial}{\partial z} \right) \quad (5)$$

and  $X_\varphi$  is the azimuthal operator

$$X_\varphi = (k_0 r)^{-2} \frac{\partial^2}{\partial \varphi^2}. \quad (6)$$

Using the Taylor expansion

$$\Psi(r + \Delta r, z, \varphi) = \exp(\Delta r \partial_r) \Psi(r, z, \varphi) \quad (7)$$

in conjunction with Eq. (3) yields a marching algorithm that forms the basis for all PE methods,

$$\Psi(r + \Delta r, z, \varphi) = \exp i\delta \left( -1 + \sqrt{1 + X_2 + X_\varphi} \right) \Psi(r, z, \varphi), \quad (8)$$

where we have set  $\delta = k_0 \Delta r$ . In its present form, Eq. (8) is unsuitable for numerical work. However, if the azimuthal coupling effects are sufficiently small, then we can approximate the full 3D propagator to  $O(\delta)$  by writing

$$\Psi(r + \Delta r, z, \varphi) \approx \exp i\delta \left( -1 + \sqrt{1 + X_\varphi} \right) \exp i\delta \left( -1 + \sqrt{1 + X_2} \right) \Psi(r, z, \varphi), \quad (9)$$

where we have used a wide-angle splitting [30,31] to separate the azimuthal operator  $X_\varphi$  from the depth operator  $X_2$ . Other splittings [32] can yield propagator approximations accurate to  $O(\delta^2)$ , but for the small effects of the azimuthal operator we restrict ourselves to Eq. (9). For  $X_\varphi \rightarrow 0$ , Eq. (9) reduces to

$$\psi(r + \Delta r, z, \varphi) = \exp i\delta \left( -1 + \sqrt{1 + X_2} \right) \psi(r, z, \varphi). \quad (10)$$

Here  $\psi$  denotes a wavefield that is independent of the azimuthal operator  $X_\varphi$ , although  $\psi$  can differ along different azimuths if  $N$  is allowed to vary with  $\varphi$ . In this case, the solutions of Eq. (10) over a range-depth computational grid for  $N$  azimuths constitute the so-called  $N \times 2D$  PE field. From Eq. (9), it is seen that 3D PE solutions involve first propagating the known PE field out from  $r$  to  $r + \Delta r$  for each azimuth using the  $N \times 2D$  propagator and then correcting this field as a function of azimuth using the azimuthal propagator. It is important to realize that for 3D calculations, azimuthal coupling must be accounted for at each range step. Even though the azimuthal operator is applied independently at each depth, the propagation from one range step to the next couples all depths together. There are many numerical PE approaches currently available for solving Eq. (9) that differ only in the treatment used to approximate the square-root operators. Most PE solution techniques involve discretizing the environment onto a regular grid in range, depth, and bearing, and then solving for the PE fields on a computational grid that can either coincide with or be offset from the environmental grid.

### A. $N \times 2D$ Propagation

In this section, we review two finite-difference procedures for solving Eq. (10). The split-step Padé PE algorithm is based on approximating the propagator in the form

$$\exp i\delta \left( -1 + \sqrt{1 + X_2} \right) \approx 1 + \sum_{m=1}^M \frac{A_m X_2}{1 + B_m X_2}. \quad (11)$$

The (complex) Padé coefficients  $A_m, B_m$  are seen to depend on  $\delta$  and can be determined in standard fashion subject to additional constraints [11] that are designed to stabilize the numerical procedures used in propagating the PE field. Using Eq. (11) in Eq. (10), we obtain the basic equation for the total one-way field

$$\psi(r + \Delta r, z, \varphi) = \psi(r, z, \varphi) + \sum_{m=1}^M \psi_m(r + \Delta r, z, \varphi), \quad (12)$$

where each partial split-step component  $\psi_m$  satisfies

$$(1 + B_m X_2) \psi_m(r + \Delta r, z, \varphi) = A_m X_2 \psi(r, z, \varphi). \quad (13)$$

Hence, the total 2D-field at range  $r + \Delta r$  is obtained by combining the current field at range  $r$  with  $M$  intermediate 2D fields  $\psi_m$  each of which depends on  $\psi(r, z, \varphi)$  through the solution of Eq. (13). A numerical advantage of this formulation is that the intermediate fields can be computed in parallel. In contrast, regular Padé PE algorithms [8] that derive from Padé approximants to the square-root operator in Eq. (10) lead to a recursive solution procedure for determining the total field at the advanced range from the partial fields. That is, substituting

$$-1 + \sqrt{1 + X_2} \approx \sum_{m=1}^M \frac{a_m X_2}{1 + b_m X_2}, \quad (14)$$

into Eq. (11) yields

$$\begin{aligned} \psi(r + \Delta r, z, \varphi) &= \prod_{m=1}^M \exp \frac{i\delta a_m X_2}{1 + b_m X_2} \cdot \psi(r, z, \varphi) \\ &\approx \prod_{m=1}^M \frac{1 + c_m^+ X_2}{1 + c_m^- X_2} \cdot \psi(r, z, \varphi), \end{aligned} \quad (15)$$

where  $c_m^\pm = b_m \pm \frac{1}{2} i\delta a_m$ . Here, the (real) Padé coefficients are given in closed form by

$$a_m = \frac{2}{2M + 1} \sin^2 \frac{m\pi}{2M + 1}, \quad b_m = \cos^2 \frac{m\pi}{2M + 1}. \quad (16)$$

For applications where numerical stability can be an issue, it is convenient to make use of complex coefficients [9,12]. It is evident that Eq. (15) admits a recursive solution in terms of  $M$  systems of the form

$$(1 + c_m^- X_2) \psi_m(r, z, \varphi) = (1 + c_m^+ X_2) \psi_{m-1}(r, z, \varphi), \quad (17)$$

where  $\psi_0(r, z, \varphi) \equiv \psi(r, z, \varphi)$  and  $\psi_M(r, z, \varphi) \equiv \psi(r + \Delta r, z, \varphi)$ . In this case, since each higher-order partial field component is based on a low-order [1/1] Padé approximant to its associated propagator, sufficiently small values of  $\delta$  are required to provide accurate solutions. Because the split-step Padé PE is based on an approximation to the propagator itself, much larger values of  $\delta$  can be used while maintaining the same level of accuracy. As a result, split-step Padé PE algorithms can be significantly more efficient than corresponding regular Padé PE methods. The PECan model contains routines for solving Eq. (10) by both the regular Padé and split-step Padé algorithms.

## B. Heterogeneous Formulation

Solutions to Eq. (13) or Eq. (17) are computed on a discrete computational grid in depth,  $z$ , range,  $r$ , and azimuth,  $\varphi$ . At each grid point, values of sound speed,  $c$ , density,  $\rho$ , and attenuation,  $\alpha$ , need to be specified. These values are often based on interpolation from a given set of environmental profiles provided at irregularly-spaced locations. Nominally, the grid is terminated above by a free (or rigid) surface at  $z = 0$  and below by an absorbing layer overlying a free (or rigid) surface at  $z = z_{\max}$ . The absorbing layer is necessary to attenuate any unwanted reflections from the base of the computational grid. The choice of  $z_{\max}$  and absorption profile  $\alpha(z)$  in this physical absorbing layer depends on the relative amount of energy that penetrates into the ocean subbottom from the ocean waveguide.

For the discretization in depth, we introduce the offset grid vector  $\mathbf{z} = [z_1, z_2, \dots, z_J]^T$ , where  $[\dots]^T$  denotes transpose and  $z_j = (j - 1/2)\Delta z$ . Use of offset depths avoids the need to compute the field along the top and bottom of the computational domain where it is known to vanish if either boundary is a free surface. In addition, the implementation of either pressure-release or rigid boundary conditions can be effected in a symmetric way. In terms of the  $\mathbf{z}$ -grid, we apply a heterogeneous approximation for  $X_2(\mathbf{z})\psi(\mathbf{z})$  in the form

$$X_2(\mathbf{z})\psi(\mathbf{z}) \approx L(\mathbf{z})\psi(\mathbf{z} - \Delta z) + D(\mathbf{z})\psi(\mathbf{z}) + U(\mathbf{z})\psi(\mathbf{z} + \Delta z), \quad (18)$$

where

$$L(\mathbf{z}) = \gamma\rho^-(\mathbf{z}), \quad U(\mathbf{z}) = \gamma\rho^+(\mathbf{z}), \quad \gamma = 1/(k_0\Delta z)^2, \quad (19)$$

$$D(\mathbf{z}) = N^2(\mathbf{z}) - 1 + L(\mathbf{z}) + U(\mathbf{z}), \quad (20)$$

$$\rho^\pm(\mathbf{z}) = 2\rho(\mathbf{z})[\rho(\mathbf{z}) + \rho(\mathbf{z} \pm \Delta z)]^{-1}. \quad (21)$$

The use of this heterogeneous form precludes the need for explicitly enforcing continuity of pressure,  $p$ , and vertical particle velocity,  $(i\omega\rho)^{-1}\partial p/\partial z$ , at any jump discontinuities in material properties—once values of  $\rho$ ,  $c$  and  $\alpha$  are specified on  $\mathbf{z}$  there are, in effect, no internal interfaces. From Eq. (21), it is observed that  $\rho^\pm(\mathbf{z}) \rightarrow 1$  for constant density media and the weighted three-term approximation to the mixed derivative term in  $X_2\psi$  reduces to the standard central-difference form.

Substituting Eq. (18) into Eq. (13) produces a tridiagonal matrix system for the split-step Padé algorithm whose  $j$ th row is given by

$$[1/B_m + X_2(z_j)] \psi_m(r + \Delta r, z_j, \varphi) = (A_m/B_m) X_2(z_j)\psi(r, z_j, \varphi). \quad (22)$$

The diagonal matrix entries in the top ( $j = 1$ ) and bottom ( $j = J$ ) rows are modified by the boundary conditions imposed along  $z = 0$  and  $z = z_{\max}$ , respectively. For a pressure-release surface, the antisymmetry of the field about  $z = 0$  is ensured by setting  $\psi_m(r, -\frac{1}{2}\Delta z, \varphi) = -\psi_m(r, z_1, \varphi)$ . This condition is implemented numerically by subtracting the  $L(z_1)$  from the diagonal entry  $D(z_1)$ . The even symmetry associated with a rigid boundary is preserved by adding  $L(z_1)$  to the diagonal entry  $D(z_1)$  instead. In a similar way, the bottom boundary condition corresponding to even (odd) symmetry about  $z = z_{\max}$  is handled by adding (subtracting)  $L(z_J)$  to (from) the diagonal entry  $D(z_J)$ .

## C. Profile Interpolation

Typical PE computational grid spacings for shallow water low-frequency predictions are of the order of 1 m in depth, 10 m in range, and  $1^\circ$  in azimuth. Environmental information for the ocean rarely exists on this scale. Thus, the acoustic modeler is faced with the issue of interpolating coarse environmental information, usually in the form of depth profiles at specified horizontal-coordinate locations, onto the computational grid.

For simplicity, consider a two-dimensional environmental configuration in the range-depth plane (single radial). The extension to include variations in three dimensions (multiple radials) is straightforward. Assume that we have

a sequence of coarse environmental profiles along a constant azimuth at the known ranges  $R_k$  km,  $k = 1, \dots, K$ . Each profile is restricted to have points at the same number of depths  $Z_\ell^k$  m,  $\ell = 1, \dots, L$ . The set of depth vertices will generally be different for each value of  $R_k$ . Here, we anticipate that the set of coarse profiles has been pre-processed to preserve significant oceanographic/geophysical features between profiles, such as the depth of the sound channel axis or surface duct and the sediment thickness beneath a sloping bathymetry. In PECan, we assume that all environmental parameters (sound speed, density, absorption) vary linearly with depth between points on a given coarse profile. Moreover, between coarse profiles, we assume that each parameter varies linearly between depth points that have the same depth index. This implies that common features between coarse profiles share the same depth index. Any discontinuities in material properties, such as occur at the sea-bottom interface, are accommodated simply by including a pair of coarse profile points that are displaced in depth by a tiny amount, e.g., 1 cm. This maneuver ensures that the set of coarse profile depths forms a monotonically increasing sequence which can be safely processed by an interpolation algorithm.

Let  $E(Z_\ell^k)$  represent the value of sound speed, density, or attenuation at the depth of the  $\ell$ th point on the coarse profile at range  $R_k$ . For an intermediate range  $R_k < R' < R_{k+1}$ , the environment on the computational grid is determined using a two-step linear interpolation procedure. First, a coarse profile at  $R'$  is obtained using

$$Z'_\ell = (1 - q)Z_\ell^k + qZ_\ell^{k+1}, \quad (23)$$

$$E(Z'_\ell) = (1 - q)E(Z_\ell^k) + qE(Z_\ell^{k+1}), \quad (24)$$

where  $q = (R' - R_k)/(R_{k+1} - R_k)$ . Values for each material property on the computational grid associated with this intermediate coarse profile are then determined using linear interpolation in depth.

For  $N \times 2D$  and  $3D$  computations, it is necessary to extend the two-step procedure outlined above to include the azimuthal coordinate. In the present version of PECan, we use a bivariate interpolation formula for finding an intermediate coarse profile at  $(R', T')$  within range  $R_k < R' < R_{k+1}$  and cross-range  $T_j < T' < T_{j+1}$  rectangular coordinates, namely

$$Z'_\ell = (1 - q)(1 - p)Z_\ell^{k,j} + q(1 - p)Z_\ell^{k+1,j} + (1 - q)pZ_\ell^{k,j+1} + qpZ_\ell^{k+1,j+1}, \quad (25)$$

$$E(Z'_\ell) = (1 - q)(1 - p)E(Z_\ell^{k,j}) + q(1 - p)E(Z_\ell^{k+1,j}) + (1 - q)pE(Z_\ell^{k,j+1}) + qpE(Z_\ell^{k+1,j+1}). \quad (26)$$

Here,  $q$  has the same meaning as given above,  $p$  is the ratio  $p = (T' - T_j)/(T_{j+1} - T_j)$ , and  $E(Z_\ell^{k,j})$  represents the value of sound speed, density, or attenuation at the depth of the  $\ell$ th point on the coarse profile at range  $R_k$  and cross-range  $T_j$ .

#### D. Energy Conservation

The derivation of the one-way propagation equation relies on factoring the Helmholtz equation into outgoing and incoming components and neglecting the coupling to the backscattered fields. Although this is formally exact only for range-independent waveguides, the algorithm is routinely applied to range-dependent cases in which the environment is modelled as a sequence of range-independent sections having different properties. That is, since the resulting propagators march the PE field step-by-step outward in range, the environment is simply updated after each range step and the coefficients implied by the terms in Eq. (13) are modified accordingly. Even for relatively benign range-dependent environments, however, this approach may not yield sufficiently accurate results [33]. The inaccuracy is related to the fact that, at abrupt changes in the environment between range sections, two boundary conditions need to be satisfied at the corresponding vertical interface in order to properly account for energy transfer along the waveguide. Of course, the one-way PE can only satisfy one boundary condition there [34]. Subsequent analysis [10] has shown, however, that if  $\psi$  is replaced by the scaled field  $\psi^* \equiv \psi/\beta$  where  $\beta = \sqrt{\rho(z)c(z)}$  in the PE algorithm, then a good approximation to the true energy-conserving condition is realized. To achieve this numerically, we replace Eq. (13) by the “energy-conserving” variant

$$\psi_m^*(r + \Delta r, z, \varphi) = \frac{A_m X_2^*}{1 + B_m X_2^*} \psi_m^*(r, z, \varphi) \quad (27)$$

where the depth operator  $X_2^*$  is defined by

$$X_2^* = N^2 - 1 + k_0^{-2} \sqrt{\frac{\rho}{\beta}} \frac{\partial}{\partial z} \left( \rho^{-1} \frac{\partial}{\partial z} \beta \right). \quad (28)$$

To illustrate the effectiveness of Eq. (28) over Eq. (13) in the case of range-varying bathymetry, we examine the penetrable wedge test case introduced as one of the Acoustical Society of America (ASA) range-dependent benchmark problems [8,33,35]. The ASA wedge geometry consists of a shallow-water shoaling waveguide in which the water depth decreases from 200 m to 0 m over a range of 4 km. The homogeneous wedge has a sound speed of  $1500 \text{ m s}^{-1}$  and a density of  $1 \text{ g cm}^{-3}$ . The fluid bottom has a constant sound speed, density and absorption of  $1700 \text{ m s}^{-1}$ ,  $1.5 \text{ g cm}^{-3}$  and  $0.5 \text{ dB } \lambda^{-1}$  respectively, so that jump discontinuities in density, sound speed, and absorption occur along the sloping line  $z = 200 - r/20 \text{ m}$ , for  $0 < r < 4000 \text{ m}$ . Calculations have been carried out at 25 Hz for a source located at  $r = 0 \text{ km}$  and  $z = 100 \text{ m}$ . Curves of transmission loss ( $-10 \log_{10} |p|^2$ ) versus range calculated for a shallow receiver at a depth of 30 m are shown in Fig. 1 and Fig. 2. The reference results (dashed lines) were obtained using the coupled mode code COUPLE [33,36]. Results obtained using PECan are shown as solid lines and were computed using  $M = 2$ ,  $\Delta z = 0.5 \text{ m}$ ,  $\Delta r = 5 \text{ m}$  and  $c_0 = 1500 \text{ m s}^{-1}$ . Both PECan calculations included an absorbing layer in the region  $500 < z < 1000 \text{ m}$  over which the attenuation ramped linearly from 0.5 to 2  $\text{dB } \lambda^{-1}$ . PECan results using Eq. (13) are given in Fig. 1 while those obtained using Eq. (28) are shown in Fig. 2. Clearly, the calculations obtained using the energy-conserving (EC) adjustment do not exhibit the extra cumulative increase in transmission losses that are observed using the non-energy-conserving (non-EC) formulation.

### E. Nonlocal Boundary Conditions

Finite-difference solutions to the PE are well-suited to handling appropriate boundary conditions at external and internal interfaces. For a water-borne source, the large impedance mismatch at the air-sea boundary ( $z = 0$ ) results in an almost perfect reflection of a sound wave with a  $180^\circ$  phase shift. Consequently, it is usually modelled in applications as a flat, pressure-release surface. However, an air-layer backing can be convenient for some PE applications involving deterministically-rough surfaces [37,38]. Internal interfaces are handled implicitly through the use of the heterogeneous approximations of Eq. (18)–Eq. (21) (suitably modified for use with the energy-conserving operator given in Eq. (28)). The traditional method of implementing the radiation condition for downgoing waves is to append an absorbing layer to the computational mesh and to set the field to zero at the base of this layer. The procedure can be inefficient for some applications, as the tapered absorption strength must increase sufficiently slowly with depth to prevent any artificial reflections due to impedance mismatches.

The approximate treatment of the downgoing radiation condition can be replaced with a nonlocal boundary condition (NLBC) that exactly transforms the original semi-infinite PE problem to an equivalent one in a bounded domain [27–29,38]. The use of such NLBC’s can significantly reduce the size of the computational domain, leading to faster numerical solutions. In addition to handling radiation into (and scattering from) a homogeneous half-space, NLBC’s can also be derived to treat the coherent scattering losses due to a rough sea-surface [21–23]. For  $N \times 2\text{D}$  computations, nonlocal boundary conditions that represent the effects of either a rough pressure-release surface at  $z = 0$  or a homogeneous penetrable bottom in  $z > z_b$ , where  $z_b$  is a depth below which the properties of the medium do not change, are available as options in PECan. For a rough free surface with Gaussian statistics, the appropriate NLBC for the standard PE (derived from the square-root approximation  $\sqrt{1 + X_2} \approx 1 + \frac{1}{2}X_2$ ) can be put in the form of the Dirichlet-to-Neumann (DtN) mapping

$$\psi_z(r, 0) = - (B_0/\sigma_0^2) \int_0^r \psi(r-t, 0) \frac{\exp ib_0 t}{\sqrt{t}} dt, \quad (29)$$

where  $B_0 = \sqrt{i/(2\pi k_0)}$ ,  $b_0 = \frac{1}{2}k_0(N_0^2 - 1)$ ,  $N_0 = N(0+)$ , and  $\sigma_0$  is the *rms* roughness along  $z = 0$ . Although this NLBC is most relevant to low-angle propagation, it can be applied to many shallow-water calculations in the far field since the steep-angle energy is usually scattered into the bottom where it is absorbed. In a similar way, at the interface above a homogeneous ocean bottom, a Neumann-to-Dirichlet (NtD) mapping for the standard PE can be derived in the form

$$\psi(r, z_b) = -B_0(\rho_b^+/\rho_b^-) \int_0^r \psi_z(r-t, z_b) \frac{\exp ib_b t}{\sqrt{t}} dt, \quad (30)$$

where  $b_b = \frac{1}{2}k_0(N_b^2 - 1)$  with  $N_b = N(z_b - 0)$  and  $\rho_b^\pm = \rho_b(z_b \pm 0)$ . Both Eq. (29) and Eq. (30) are derived under the assumption that the vertical wavenumber associated with the PE field near the respective interfaces is adequately approximated by the vertical wavenumber that corresponds to the standard PE. Although this approximation implies that these NLBC’s are mismatched when combined with higher-order split-step Padé propagators, numerical testing has indicated that these low-order NLBC’s give good results in many cases of interest [22,23]. Although nonlocal boundary conditions satisfied by the third-order Claerbout PE [39] (obtained when  $M = 1$  by setting  $A_1 = \frac{1}{2}i\delta$  and

$B_1 = \frac{1}{4}(1 - i\delta)$  in Eq. (11), or equivalently,  $a_1 = \frac{1}{2}$  and  $b_1 = \frac{1}{4}$  in Eq. (14)) and the exact one-way PE in Eq. (10) have been derived and implemented elsewhere [22,23,28], they have not yet been incorporated into PECan. At present, the option of applying either Eq. (29) or Eq. (30) (or both) to higher-order solutions of Eq. (13) or Eq. (18) are available.

For the ASA wedge example, the results of replacing the absorbing layer with nonlocal boundary conditions applied along  $z = 250$  m are shown in Fig. 3 and Fig. 4. In this case, the depth extent of the computational grid was decreased by a factor of four. The PECan+NLBC transmission losses shown in Fig. 3 for the shallow receiver are observed to agree closely with those in Fig. 2 obtained using PECan with the absorbing layer. In addition, the corresponding CPU time decreased by a factor of three. The calculations for the 150-m receiver are shown in Fig. 4 and while there is good agreement overall between transmission loss curves, the PECan+NLBC results are observed to depart from the COUPLE results in the vicinity of the high-loss null near a range of 3 km. The agreement in this region is expected to improve for a nonlocal boundary condition based on Claerbout's PE [28].

As mentioned above, NLBC's can also be used to incorporate the extra scattering losses in the coherent component of the propagating fields due to a rough surface. To examine this feature, we consider the shallow-water Pekeris waveguide that was introduced at a 1981 PE Workshop as Test Case 3 [40]. The region  $0 < z < 100$  m contains a homogeneous fluid with sound speed  $1500 \text{ m s}^{-1}$  and density  $1 \text{ g cm}^{-3}$  that overlays a fluid half-space with constant sound speed, density and absorption of  $1590 \text{ m s}^{-1}$ ,  $1.2 \text{ g cm}^{-3}$  and  $0.5 \text{ dB } \lambda^{-1}$ , respectively. The 250-Hz source frequency gives rise to 11 propagating modes in this waveguide. Both the source and the receiver are located at mid-depth (50 m) in the upper layer. We compute predictions of transmission loss for both a flat-surface and one characterized by a zero-mean, Gaussian surface with an *rms* roughness of 4 m. For this range-independent example, we compare our results to reference results obtained using SAFARI [41], a well-known spectral model based on wavenumber integration that includes a capability for modelling rough boundaries [42,43].

The results of applying PECan with nonlocal boundary conditions to the Pekeris waveguide are displayed in Fig. 5 for the flat-surface case and in Fig. 6 for the rough-surface case. For both PECan calculations, we used  $M = 4$ ,  $\Delta z = 0.125 \text{ m}$ ,  $\Delta r = 5 \text{ m}$  and applied an NLBC along the interface at  $z = 100 \text{ m}$  to handle reflection/transmission effects due to the bottom half-space. The flat-surface PECan results shown in Fig. 5 are indistinguishable from the SAFARI results. For the rough-surface problem, PECan was also used with the NLBC of Eq. (29) applied along  $z = 0 \text{ m}$ . Again, the agreement with the SAFARI prediction is excellent. At this frequency, the 4 m *rms* surface roughness is observed to have a considerable effect on the propagating waves. Due to the stripping of the higher-order modes, the transmission loss results are considerably smoother and the overall losses have increased by several dB.

## F. Shear

The current focus on shallow water propagation, where the physics of bottom interaction must be taken into account, implies that PE models must be capable of treating the influence of shear rigidity in the sediments. Although a fully elastic PE model could be employed for this purpose [12,13], it is desirable from an efficiency standpoint to have a less computationally intensive solution. Fortunately, for many problems, it is possible to represent the effects of shear on the propagation in the water column through use of an "equivalent" fluid approximation [25,44]. The approach is based on choosing fluid parameters to match the reflection coefficient of the actual solid bottom. One way to achieve this is to convert the shear parameters into a complex density of the form

$$\rho'_b = \rho_b \left[ \left(1 - 2/N_s^2\right)^2 + \frac{4i\gamma_s\gamma_b}{k_0^2 N_s^4} \right], \quad (31)$$

where  $\rho_b$  is the true value of density in the sediment,  $N_s = (c_0/c_s)(1 + i\alpha_s)$ , and  $c_s$  and  $\alpha_s$  are the sediment shear speed and attenuation, respectively. In Eq. (31), the quantities  $\gamma_s = k_0\sqrt{N_s^2 - 1}$  and  $\gamma_b = ik_0\sqrt{1 - N_b^2}$  are the respective vertical wavenumbers of the shear and compressional waves in the sediments. Choosing the density to be complex in this way allows the plane-wave reflection coefficient of the fluid-elastic sub-bottom to be approximated by the reflection coefficient of an equivalent fluid for a range of angles that correspond to the propagating modes. Although the value of  $c_0$  may require adjustment to optimize the matching (it is a free parameter), this does not significantly affect high-order PE algorithms which are inherently capable of modelling wide-angle propagation and, hence, insensitive to the value of  $c_0$  that is chosen.

For an elastic half-space, the complex density can be directly incorporated into the nonlocal boundary condition in Eq. (30). To demonstrate this capability, we introduce a further modification to the Pekeris waveguide problem in which the fluid half-space  $z > 100 \text{ m}$  is replaced with a solid half-space having the same values of compressional speed and compressional absorption, but with values of shear speed and shear absorption given by  $500 \text{ m s}^{-1}$  and  $1 \text{ dB}/\lambda$ , respectively. To enhance the bottom interaction, we consider propagation between a source and receiver placed at a

depth of 99.5 m. Difficulties associated with truncating a vertically extended PE source field (see, e.g., [3]) placed adjacent to the bottom interface were avoided by extending the depth at which the NLBC is applied to 110 m.

Transmission loss comparisons for the 99.5-m source-receiver pair in the Pekeris waveguide are given in Fig. 7 for the fluid-bottom case and in Fig. 8 for the solid-bottom case. For both PECan calculations, we used  $M = 4$ ,  $\Delta z = 0.125$  m,  $\Delta r = 5$  m,  $c_0 = 1530$  m s<sup>-1</sup>, and a NLBC applied 10 m below the sea-bottom interface to absorb downgoing radiation in  $z > 110$  m. For both the fluid and solid bottoms, the PECan results are observed to be in good agreement with the SAFARI results. For the near-bottom placement of the source and receiver in this problem, the equivalent fluid approximation is seen to account accurately for the significant loss of energy (several dB) due to shear wave propagation in the solid. Moreover, the equivalent bottom accommodates the phase changes in the propagating modes that alter the interference pattern of the transmission loss curve. The slight departure in level that is observed between the PECan and SAFARI curves is due to the use of a simple starting field—it does not take the influence of the geoacoustics of the bottom into account. This aspect of propagation due to a near-bottom source is described next.

### G. Self-starter

Before a PE algorithm can advance the solution of a one-way equation outward in range, an initial condition (starting field) is required at the range of the source. In addition to the simple PE starting fields [2,3,35,45] that approximate asymptotically the field due to a point source, PECan also includes an option for generating the so-called self-starter [26]. The self-starter initial field is determined by solving

$$\sqrt{1 + X_2} \cdot \psi(0, z) = -\frac{1}{2}(i/k_0)\delta(z - z_s), \quad (32)$$

where  $z_s$  is the depth of the source and  $\psi(0, z)$  is the starting field at  $r = 0$ . Whereas the simple starting fields only model the environment as a homogeneous half-space, the self-starter contains all of the environmental information in the vicinity of the source. Different procedures for solving Eq. (32) numerically derive from various formulations used to represent the square-root operator. In PECan, we use the standard PE approximation  $\sqrt{1 + X_2} \approx 1 + \frac{1}{2}X_2$  in Eq. (32) to obtain

$$(2 + X_2) \psi(0, z) = -(i/k_0)\delta(z - z_s). \quad (33)$$

Specialized, but straightforward techniques are then used to solve Eq. (33) within a heterogeneous finite-difference framework.

The self-starter is most important for near-field calculations, although it can be important for obtaining the correct far-field levels for sources that are placed near the sea-bottom. To illustrate this latter behaviour, we consider another modified version of the Pekeris fluid waveguide problem. The modifications to the original NORDA 3 problem this time involve placing the source-receiver pair right on the sea-bottom interface at  $z = 100$  m and increasing the density in the lower half-space from  $1.2$  g cm<sup>-3</sup> to  $2$  g cm<sup>-3</sup> [3]. Transmission loss comparisons for this problem are shown in Fig. 9 between SAFARI and PECan where the PE calculation was initialized using a simple starting field due to Green [45]. It is evident that the level of the transmission loss curve is displaced from the reference curve by a constant value of about 2.5 dB. In contrast, the transmission loss curve shown in Fig. 10 obtained with the self-started PE source field is indistinguishable from the SAFARI curve. It can be shown that the use of the self-starter also shifts the PECan curves in Fig. 7 and Fig. 8 into near-perfect alignment with the SAFARI curves.

### H. 3D Coupling

3D parabolic equation models have been developed by several authors for modelling the effects of three-dimensional oceanographic features on acoustic propagation [46–52]. In this section, we extend the finite-difference procedure for solving the 2D PE to accommodate azimuthal variations by considering (recall Eq. (9) and Eq. (10))

$$\Psi(r + \Delta r, z, \varphi) = \exp i\delta \left( -1 + \sqrt{1 + X_\varphi} \right) \psi(r + \Delta r, z, \varphi). \quad (34)$$

The exponential azimuthal operator can be handled using either discrete Fourier transforms (DFT's) or finite-differences. Essentially,  $\psi(r + \Delta r, z, \varphi)$  represents the 2D PE field at range  $r + \Delta r$  on a grid of points in depth and azimuth. In order to compute the full 3D PE field, Eq. (34) must be solved at every point in the depth grid

over all azimuths. PECan is currently configured to compute azimuthal coupling contributions over a full 360°-sector. Applying DFT's to Eq. (34) yields the solution

$$\Psi(r + \Delta r, z, \varphi) = \mathcal{F}_\varphi^{-1} \left\{ \exp i\delta \left( -1 + \sqrt{1 - \kappa^2} \right) \cdot \mathcal{F}_\varphi \{ \psi(r + \Delta r, z, \varphi) \} \right\} \quad (35)$$

where  $k_0^2 \kappa^2 = k_\varphi^2 [r(r + \Delta r)]^{-1}$ ,  $\mathcal{F}_\varphi\{\cdot\}$  denotes the DFT from  $\varphi$ -space to  $k_\varphi$ -space and  $\mathcal{F}_\varphi^{-1}\{\cdot\}$  denotes its inverse transform. At each range step, the 3D coupling involves computing a DFT pair and applying a multiplicative operator at each point on the depth grid.

Alternatively, the finite difference solution of Eq. (34) requires that we first find a representation for  $\exp i\delta \left( -1 + \sqrt{1 + X_\varphi} \right)$  that is amenable to finite-difference treatments. Although it is possible to use a higher-order Padé representation for this purpose, since  $X_\varphi$  is assumed to be small, PECan makes use of a low-order [1/1] Padé approximation to the square-root operator followed by a rational-linear approximation to the propagator to obtain

$$\begin{aligned} \Psi(r + \Delta r, z, \varphi) &\approx \exp \frac{\frac{1}{2}i\delta X_\varphi}{1 + \frac{1}{4}i\delta X_\varphi} \cdot \psi(r + \Delta r, z, \varphi) \\ &\approx \frac{1 + \frac{1}{4}(1 + i\delta)X_\varphi}{1 + \frac{1}{4}(1 - i\delta)X_\varphi} \cdot \psi(r + \Delta r, z, \varphi), \end{aligned} \quad (36)$$

which can be written in the equivalent form,

$$\left( 1 + \frac{1}{4} - \frac{1}{4}i\delta X_\varphi \right) \Psi(r + \Delta r, z, \varphi) = \left( 1 + \frac{1}{4} + \frac{1}{4}i\delta X_\varphi \right) \psi(r + \Delta r, z, \varphi). \quad (37)$$

The implicit Crank-Nicolson form in Eq. (37) can be solved on a discrete grid using standard finite-difference approximations.

To illustrate the effect of azimuthal coupling, we consider  $N \times 2D$  and 3D propagation for a penetrable wedge problem that was examined previously by Fawcett [50]. The Fawcett wedge is based on a modification to the 2D ASA wedge configuration discussed above. The original ASA geometry is continued downslope until a range of 3.6 km is reached at which point the waveguide becomes range independent with a water depth of 380 m. Similarly, at an upslope range of 3.6 km, the sloping waveguide is terminated with a range independent section of depth 20 m. A 25-Hz point source is situated at range  $r = 0$  km and depth  $z = 100$  m above the sloping bottom where the water depth is  $z_b = 200$  m. We choose the  $\varphi = 0^\circ$  azimuth to align with the upslope direction. The 2D wedge is invariant along the  $\varphi = 90^\circ$  and the  $\varphi = 270^\circ$  azimuths. The resulting acoustic fields are symmetric about the upslope direction. Because the coherent field behaviour due to a point source can be very complicated even for such a simple bathymetric geometry, we choose to examine the  $N \times 2D$  and 3D fields that are excited by a single mode of the form

$$\psi_2(0, z, \varphi) = \begin{cases} \sin(\gamma_w z) & \text{for } 0 \leq z \leq z_b \\ \sin(\gamma_w z_b) \exp -\gamma_b(z - z_b) & \text{for } z > z_b \end{cases} \quad (38)$$

Here  $\gamma_w = \sqrt{\omega^2/c_w^2 - k_n^2}$  and  $\gamma_b = \sqrt{k_n^2 - \omega^2/c_b^2}$  are vertical wavenumbers of the field in  $z < z_b$  and  $z > z_b$ , respectively, for the  $n$ th modal wavenumber  $\omega/c_b < k_n < \omega/c_w$  that satisfies the characteristic equation for a Pekeris waveguide having the Fawcett wedge parameters at  $r = 0$  km (see [51] for details). For the calculations to follow, we initiated PECan using Eq. (34) for  $n = 3$  where  $k_3 = 0.0962252$  rad  $m^{-1}$ . All calculations for this example were carried out using  $\Delta z = 1$  m,  $\Delta r = 100$  m, and  $M = 4$  for 2048 azimuths with  $c_0 = 1632$  m  $s^{-1}$  (corresponding to the phase speed for mode 3 at the source location). For comparison, we validate our results against those generated using Fawcett's 3D PE code FawPE [50,51].

To show a full azimuthal comparison, we display gray-scale images of the transmission loss (at a receiver depth of 36 m) as a function of range and azimuth in Fig. 11 for the  $N \times 2D$  calculations and in Fig. 12 for the 3D calculations. For this geometry, both fields are symmetric about the upslope ( $\varphi = 0^\circ$ ) direction so only the results in a 180°-sector are shown. The 3D result in Fig. 12 clearly exhibits horizontal refraction of energy into the region just downslope from the cross-slope direction (along the  $\varphi = 270^\circ$  azimuth) that is not evident in the  $N \times 2D$  result in Fig. 11. This behaviour is typical of propagation across sloping bathymetry and has been observed experimentally using a towed array off a continental shelf environment [53]. The differences in transmission loss observed between the  $N \times 2D$  and 3D results decrease for receivers away from the cross-slope direction.

In Fig. 13, we display transmission loss-versus-range curves for a receiver at a depth of 36 m along  $\varphi = 90^\circ$ , i.e., the cross-slope azimuth corresponding to the 200 m isobath. PECan results for both  $N \times 2D$  (no azimuthal coupling) and 3D (full azimuthal coupling) are shown. The departure of the 3D curve from the  $N \times 2D$  curve near a range of 12 km illustrates the importance of azimuthal coupling in this case. In Fig. 14, we compare our 3D PECan results to

the corresponding results generated using FawPE. The good agreement between the PECan and FawPE transmission losses well into the shadow region indicates the viability of PECan in its accounting of such coupling. For the upslope (downslope) transmission loss comparisons shown in Fig. 15 (Fig. 16), almost no differences can be observed at a receiver depth of 36 m. Finally, the comparisons of azimuthal transmission losses along circular arcs at  $r = 5$  km and  $r = 15$  km given in Fig. 17 and Fig. 18, respectively, reveal that these azimuthal differences become more localized to the cross-slope direction with increasing range from the source.

### III. SWAM'99 RESULTS

In this section, we present results obtained with PECan for several selected CW test cases introduced at the SWAM'99 workshop. A more detailed comparison of PECan results with results from other models is presented elsewhere [24]. Typically, transmission loss as a function of range, depth or azimuth for a given source and receiver combination is used as the performance measure. Results for  $N \times 2D$  and 3D problems are also displayed in the form of images of transmission loss versus range and azimuth at a fixed receiver depth.

#### A. Test Case 1

One criterion underlying the selection of the SWAM'99 test cases was to examine the method of range interpolation used in a range-varying environment. Test Case 1 (Flat) consisted of several sets of ten different 2D coarse profiles spaced at roughly 2-km intervals along a 20-km track. Each environmental set is characterized by an isospeed ocean ( $1500 \text{ m s}^{-1}$ ) overlaying 10 2-km bottom sections with differing geoacoustic parameters in each range section, e.g., compressional speed gradients and shear rigidity. The water depth of each section is 100 m. The question of how the geoacoustic parameters in the bottom should be interpolated within each range section was left unresolved and provided an additional degree of freedom for each acoustic modeler to consider. The simplest method is to keep the environmental parameters fixed between given coarse profiles, that is, without any range interpolation (non-RI). An alternate method is to apply the range interpolation (RI) scheme specified in Eq. (23) between each pair of input profiles. PECan calculations were carried out using both RI and non-RI methods. In this section, we compare transmission loss results for Test Cases 1a and 1c.

Test Case 1a is characterized by a low value of compressional speed for the sediment at the water-bottom interface ( $1487.04 \text{ m s}^{-1}$ ). In contrast, the surficial sediment compressional speed for Test Case 1c is much higher ( $1688.53 \text{ m s}^{-1}$ ). In Fig. 19 and Fig. 20 we display transmission losses versus depth at a range of 15 km for Test Cases 1a and 1c, respectively, comparing RI results (dashed line) to non-RI results (solid line). The results shown in these figures were computed using the energy conservation (EC) option for  $\Delta r = 10$  m,  $\Delta z = 0.5$  m,  $M = 4$  and included a 500-m absorbing bottom layer (recall that an NLBC cannot be applied in a range-varying layer or one that contains sound-speed gradients). It is evident from these results that the effects of range interpolation are much more significant for the slow-speed bottom (Fig. 19) than for the high-speed bottom (Fig. 20). This behaviour is also evident in the transmission losses versus range results for a receiver at a depth of 35 m given in Fig. 21 for Test Case 1a and in Fig. 22 for Test Case 1c. Because of the low compressional speed in the ocean bottom in Test Case 1a, when range interpolation is not invoked, more energy is coupled into the ocean bottom within the first 2-km range section. When range interpolation is applied, however, the higher bottom speed and upward-refracting sound speed gradient in the second range segment causes the interpolated bottom compressional speed to increase rapidly with range. As a result, sound energy that was transmitted into the low-speed medium with the non-RI approach becomes trapped and is subsequently returned to the water column with the RI method. This effect is much less noticeable for Test Case 1c since the sea-bottom sound speeds in the vicinity of the source are larger than that in the water column and a greater proportion of energy is trapped at short ranges. In summary, range interpolation of coarse environmental information onto the fine-scale computational grids can have a significant effect on PE model predictions for range-dependent propagation problems.

#### B. Test Cases 2 & 3

Test Case 2 (Down) and Test Case 3 (Up) combine 2D range-dependent bathymetry with range-varying environments similar to the Flat ones considered in Test Case 1 and provide an opportunity to check the capability of PECan to preserve reciprocity. In particular, the transmission loss between a receiver at range  $r_0$  km and depth 35 m due to a source at range 0 km and depth 30 m for Test Case 2c should exactly equal the transmission loss between a receiver

at range  $r_0$  km and depth 30 m due to a source at range 0 km and depth 35 m for Test Case 3c. To ensure a proper check on reciprocity in this instance, the environmental configuration for the Down waveguide geometry must exactly mirror the environmental configuration of the Up waveguide geometry. In order to meet this requirement for this comparison, we must use  $r_0 = 18$  km for the RI results instead of  $r_0 = 20$  km that was used for the non-RI results. Reciprocal transmission losses obtained with PECan are presented in Fig. 23 and Fig. 24 for the non-RI method and in Fig. 25 and Fig. 26 for the range interpolated method. Non-EC results are shown in Fig. 25 and Fig. 27 while energy conserved results are given in Fig. 26 and Fig. 28. The absolute value of the difference in transmission loss values ( $\Delta$ ) observed between each pair of curves are displayed at the appropriate reciprocal point on each figure. These PECan results were generated using the computational parameters  $\Delta z = 0.5$  m,  $\Delta r = 10$  m, and  $M = 4$ .

The non-RI results given in Fig. 23 and Fig. 24 indicate that reciprocity is approximately satisfied ( $\Delta \sim 1$  dB) whether or not energy conservation is invoked. A simple explanation for this behaviour is that, in the absence of range interpolation, there are only 10 vertical interfaces across which the PE-field needs to be corrected for energy conservation. Evidently, the relatively small number of interfaces encountered in non-RI calculations for this test case pair do not contribute significantly to any loss (gain) of energy as the field is marched upslope (downslope).

For the RI curves shown in Fig. 25 and Fig. 26, however, large departures are observed between the EC and non-EC reciprocity values. For the case of range interpolation, the field is corrected at each PE range step. As the number of interfaces increases, the cumulative departure between EC and non-EC reciprocity values increases. We note that the best reciprocal behaviour is exhibited by the energy conserving and range interpolated results (to within 0.3 dB). The poorest reciprocal agreement occurs for range interpolated results when energy conservation is not applied.

### C. Test Case 4

Test Case 4b (Synthetic Canyon) involves 3D propagation in the vicinity of a bathymetric canyon-type feature. The canyon depth,  $z_b$  (m), as a function of range,  $r$  (km), along the  $R$  coordinate ( $\varphi = 0^\circ$ ) is parameterized by the analytical bathymetric function  $z_b(r) = 200 + 500 \exp -\frac{1}{2}(r - 10)^2$ . This 2D feature is then extended uniformly in the cross-range coordinate  $T$ . A 25-Hz source is situated at a depth of 30 m midway across the canyon. For this geometry, the resulting  $N \times 2D$  and 3D acoustic fields are symmetric about both the cross-canyon and along-canyon directions. The ensuing calculations for this case were generated using  $\Delta z = 1$  m,  $\Delta r = 100$  m, for  $M = 4$  and 2048 azimuths.

The effects of azimuthal coupling between  $N \times 2D$  and 3D propagation for this canyon test case can be seen by comparing the grey-scale images displayed in Fig. 27 and Fig. 28. Because of symmetry, only a portion of the azimuthal fields are displayed. The  $N \times 2D$  results are displayed in Fig. 27 and the 3D results are displayed in Fig. 28 for a receiver depth of 35 m. The significant differences between the uncoupled and coupled results that are evident along the canyon axis are a result of the substantial focussing of acoustic energy by the sidewalls of the canyon when azimuthal coupling is taken into account. Transmission losses versus range along the  $\varphi = 0^\circ$  (across canyon) and  $\varphi = 90^\circ$  (along canyon) radials are shown in Fig. 29 and Fig. 30, respectively, for a receiver at a depth of 35 m. Both  $N \times 2D$  (dashed line) and 3D (solid line) PECan results are displayed. Although there is no reference solution available for this problem, a significant enhancement of acoustic levels along the axis of the canyon is observed when 3D coupling effects are taken into account. In contrast, the 3D coupling effects are not nearly as evident for the across canyon results.

Finally, we compare in Fig. 31 and Fig. 32,  $N \times 2D$  and 3D transmission losses along the quarter-circle arcs at ranges of  $r = 5$  km and  $r = 15$  km, respectively. Although the overall transmission loss levels at these ranges are similar, it is clear that horizontal refraction of sound significantly alters the phasing of the modal interference patterns observed at all angles away from the cross canyon ( $\varphi = 0^\circ$ ) direction.

## IV. SUMMARY

In this paper, the  $N \times 2D/3D$  underwater acoustics propagation model PECan (**C**anadian **P**arabolic **E**quation) was introduced, validated against standard benchmark solutions, and applied to some test cases that were offered for numerical consideration at the SWAM'99 shallow water acoustics modelling workshop [24]. It is based on high-order finite-difference Padé approximations to the 2D depth-dependent pseudo-differential operator with provisions to accommodate: energy conservation (needed to prevent extra transmission loss (gain) in upslope (downslope) situations for range-dependent problems); nonlocal boundary conditions (for treating either the reflection losses due to a stably-rough ocean (free) surface or the reflection/transmission effects due to a homogeneous ocean bottom); shear rigidity in ocean sediments (through the use of an equivalent fluid approximation that results in a complex density); a self-starter initial field algorithm (important when the source is placed on or near the ocean bottom);

and, full 3D azimuthal coupling approximations (to accommodate horizontal refraction effects, e.g., due to sloping bathymetry typically found in continental shelf environments, that cannot be accounted for using an  $N \times 2D$  model).

A comparison of PECan results to other  $N \times 2D/3D$  models results for a suite of single-frequency test cases is summarized elsewhere [24]. Herein, we focussed on presenting the underlying theory of PECan with emphasis on several modifications that have been incorporated to accommodate recent advances in PE modelling capability. These enhancements to PECan were validated by comparing 2D transmission loss predictions to predictions obtained using standard benchmark models (COUPLE, SAFARI) for several well-known test cases adapted from the underwater acoustics literature. For validation of PECan's  $N \times 2D/3D$  capability, we chose to compare our results to those obtained using another PE model implementation (FawPE). In this case, we examined the field about a 2D penetrable wedge excited by a single mode. Subsequently, we presented some results for a few selected cases taken from the SWAM'99 workshop. In particular, we examined the effects of range interpolated (RI) versus non-RI calculations, for both energy conserved (EC) and non-EC options. It was found that the RI+EC combination gave the best agreement when reciprocity was checked for an upslope/downslope range-varying environment. Finally, pronounced 3D azimuthal coupling was observed in the fields that were computed for a synthetic canyon test case due to a point source located in the center of the canyon.

The version of PECan described herein is intended to undergo regular upgrades to incorporate significant advances in PE modelling capability. The aim is to produce and maintain a robust PE-based  $N \times 2D/3D$  acoustic modelling code for ongoing application to a wide range of problems in underwater sound propagation within Canada's three ocean environments.

- 
- [1] A. Tolstoy, *Matched Field Processing in Underwater Acoustics*. World Scientific, Singapore, 1993.
  - [2] F. D. Tappert, The parabolic approximation method, in *Wave Propagation and Underwater Acoustics*. J. B. Keller and J. S. Papadakis, eds. Springer, New York, 1977, pp. 224–287.
  - [3] F. B. Jensen, W. A. Kuperman, M. B. Porter and H. Schmidt, *Computational Ocean Acoustics*. AIP Press, New York, 1994.
  - [4] D. Lee and S. T. McDaniel, Ocean acoustic propagation by finite-difference methods, *Comput. Math. Appl.* **14** (1987) 305–423.
  - [5] M. D. Collins, Higher-order, energy-conserving, two-way, and elastic parabolic equations, in *PE Workshop II: Proceedings of the Second Parabolic Equation Workshop*. S. A. Chin-Bing, D. B. King, J. A. Davis and R. B. Evans, eds. US Government Printing Office, Washington, DC, 1993, pp. 145–168.
  - [6] M. D. Collins, R. J. Cederberg, D. B. King and S. A. Chin-Bing, Comparison of algorithms for solving parabolic wave equations, *J. Acoust. Soc. Am.* **100** (1996) 178–182.
  - [7] A. Bamberger, B. Engquist, L. Halpern and P. Joly, Higher order paraxial wave equation approximations in heterogeneous media, *SIAM J. Appl. Math.* **48** (1988) 129–154.
  - [8] M. D. Collins, Benchmark calculations for higher-order parabolic equations, *J. Acoust. Soc. Am.* **87** (1990) 1535–1538.
  - [9] F. A. Milinazzo, C. A. Zala and G. H. Brooke, Rational square-root approximations for parabolic equation algorithms, *J. Acoust. Soc. Am.* **101** (1997) 760–766.
  - [10] M. D. Collins and E. K. Westwood, A higher-order energy-conserving parabolic equation for range-dependent ocean depth, sound speed, and density, *J. Acoust. Soc. Am.* **89** (1991) 1068–1075.
  - [11] M. D. Collins, The split-step Padé solution for the parabolic equation method, *J. Acoust. Soc. Am.* **93** (1993) 1736–1742.
  - [12] M. D. Collins, A higher-order parabolic equation for wave propagation in an ocean overlying an elastic bottom, *J. Acoust. Soc. Am.* **86** (1989) 1459–1464.
  - [13] B. T. R. Wetton and G. H. Brooke, One-way wave equations for seismoacoustic propagation in elastic waveguides, *J. Acoust. Soc. Am.* **87** (1990) 624–632.
  - [14] M. D. Collins, Higher-Order Padé approximations for accurate and stable elastic parabolic equations with application to interface wave propagation, *J. Acoust. Soc. Am.* **89** (1991) 1050–1057.
  - [15] M. D. Collins and R. B. Evans, A two-way parabolic equation for acoustic backscattering in the ocean, *J. Acoust. Soc. Am.* **91** (1992) 1357–1368.
  - [16] G. H. Brooke and D. J. Thomson, A single-scatter formalism for improving PE calculations in range-dependent media, in *PE Workshop II: Proceedings of the Second Parabolic Equation Workshop*. S. A. Chin-Bing, D. B. King, J. A. Davis and R. B. Evans, eds. US Government Printing Office, Washington, DC, 1993, pp. 126–144.
  - [17] M. D. Collins, A two-way parabolic equation for elastic media, *J. Acoust. Soc. Am.* **93** (1993) 1815–1825.
  - [18] M. D. Collins, W. A. Kuperman and W. L. Siegmann, A parabolic equation for poro-elastic media, *J. Acoust. Soc. Am.* **98** (1995) 1645–1656.

- [19] M. D. Collins, J. F. Lingeitch and W. L. Siegmann, Wave propagation in poro-acoustic media, *Wave Motion* **25** (1997) 265–272.
- [20] J. F. Lingeitch and M. D. Collins, Wave propagation in range-dependent poro-acoustic waveguides, *J. Acoust. Soc. Am.* **104** (1998) 783–790.
- [21] D. J. Thomson and G. H. Brooke, Non-local boundary conditions for 1-way wave propagation, in *4th International Conference on Mathematical and Numerical Aspects of Wave Propagation*. J. A. DeSanto, ed. SIAM, Golden, CO 1998, pp. 348–352.
- [22] G. H. Brooke and D. J. Thomson, Non-local boundary conditions for high-order PE models with application to scattering from a rough surface, Tech. Memo. DREA TM 1999–121, Defence Research Establishment Atlantic, Dartmouth, NS (1999).
- [23] G. H. Brooke and D. J. Thomson, Non-local boundary conditions for higher-order parabolic equation algorithms, *Wave Motion* **31** (2000) 117–129.
- [24] K. B. Smith and A. Tolstoy, Summary of results for SWAM’99 test cases, *SWAM’99: Proceedings of a Shallow Water Acoustic Modeling Workshop*. Springer, New York, 2000.
- [25] Z. Y. Zhang and C. T. Tindle, Improved equivalent fluid approximations for a low shear speed ocean bottom, *J. Acoust. Soc. Am.* **98** (1995) 3391–3396.
- [26] M. D. Collins, A self-starter for the parabolic equation method, *J. Acoust. Soc. Am.* **92** (1992) 2069–2074.
- [27] J. S. Papadakis, M. I. Taroudakis, P. J. Papadakis and B. Mayfield, A new method for a realistic treatment of the sea bottom in the parabolic approximation, *J. Acoust. Soc. Am.* **92** (1992) 2030–2038.
- [28] J. S. Papadakis, Exact, nonreflecting boundary conditions for parabolic-type approximations in underwater acoustics, *J. Comp. Acoust.* **2** (1994) 83–98.
- [29] D. J. Thomson and M. E. Mayfield, An exact radiation condition for use with the *a posteriori* PE method, *J. Comp. Acoust.* **2** (1994) 113–132.
- [30] M. D. Feit and J. A. Fleck, Jr., Light propagation in graded-index fibers, *Appl. Opt.* **17** (1978) 3990–3998.
- [31] D. J. Thomson and N. R. Chapman, A wide-angle split-step algorithm for the parabolic equation, *J. Acoust. Soc. Am.* **74** (1983) 1848–1854.
- [32] F. D. Tappert and R. H. Hardin, Computer simulation of long-range ocean acoustic propagation using the parabolic equation method, in *Proceedings of the 8th International Congress on Acoustics, Vol. 2*. Goldcrest, London, UK 1974, p. 452.
- [33] F. B. Jensen and C. M. Ferla, Numerical solution of range-dependent benchmark problems in ocean acoustics, *J. Acoust. Soc. Am.* **87** (1990) 1499–1510.
- [34] M. B. Porter, F. B. Jensen and C. M. Ferla, The problem of energy conservation in one-way models, *J. Acoust. Soc. Am.* **89** (1991) 1058–1067.
- [35] D. J. Thomson, Wide-angle parabolic equation solutions to two range-dependent benchmark problems, *J. Acoust. Soc. Am.* **87** (1990) 1514–1520.
- [36] R. B. Evans, A coupled mode solution for acoustic propagation in a waveguide with stepwise depth variations of a penetrable bottom, *J. Acoust. Soc. Am.* **74** (1983) 188–195.
- [37] D. J. Thomson, G. H. Brooke and E. S. Holmes, PE approximations for scattering from a rough surface, Tech. Memo. 95–21, Defence Research Establishment Pacific, Victoria, BC (1995).
- [38] D. Yevick and D. J. Thomson, Nonlocal boundary conditions for finite-difference parabolic equation solvers, *J. Acoust. Soc. Am.* **106** (1999) 143–150.
- [39] J. F. Claerbout, Coarse grid calculations of waves in inhomogeneous media with application to delineation of complicated seismic structure, *Geophysics* **35** (1970) 407–418.
- [40] J. A. Davis, D. White, and R. C. Cavanagh, *NORDA Parabolic Equation Workshop, 31 March–3 April, 1981*. Tech. Note 143, Naval Ocean Research and Development Activity, NSTL Station, MS (1982).
- [41] H. Schmidt, SAFARI Seismo-Acoustic Fast field Algorithm for Range-Independent environments, Report SR–113, SACLANTCEN ASW Research Centre, San Bartolomeo, Italy (1988).
- [42] W. A. Kuperman, Coherent component of specular reflection and transmission at a randomly rough two-fluid interface, *J. Acoust. Soc. Am.* **58** (1975) 365–370.
- [43] H. Schmidt and W. A. Kuperman, Rough surface elastic wave scattering in a horizontally stratified ocean, *J. Acoust. Soc. Am.* **79** (1986) 1767–1777.
- [44] J.-F. Li and M. Hodgson, Development and evaluation of equivalent-fluid approximations for sea-bottom sound reflection, *Can. Acoust.* **26(1)** (1998) 3–11.
- [45] R. R. Greene, The rational approximation to the acoustic wave equation with bottom interaction, *J. Acoust. Soc. Am.* **76** (1984) 1764–1773.
- [46] R. N. Baer, Propagation through a three-dimensional eddy including effects on an array, *J. Acoust. Soc. Am.* **69** (1981) 70–75.
- [47] J. S. Perkins and R. N. Baer, An approximation to the three-dimensional parabolic-equation method for acoustic propagation, *J. Acoust. Soc. Am.* **72** (1982) 515–522.
- [48] M. D. Collins and S. A. Chin-Bing, A three-dimensional parabolic equation model that includes the effects of rough boundaries, *J. Acoust. Soc. Am.* **87** (1990) 1104–1109.

- [49] D. Lee, G. Botseas and W. L. Siegmann, Examination of three-dimensional effects using a propagation model with azimuthal coupling capability, *J. Acoust. Soc. Am.* **91** (1992) 3192–3202.
- [50] J. A. Fawcett, Modeling three-dimensional propagation in an oceanic wedge using parabolic equation methods, *J. Acoust. Soc. Am.* **93** (1993) 2627–2632.
- [51] F. B. Sturm and J. A. Fawcett, Numerical simulation of the effects of bathymetry on underwater sound propagation using three-dimensional parabolic models, Report SM-342, SACLANTCEN ASW Research Centre, San Bartolomeo, Italy (1998).
- [52] K. B. Smith, A three-dimensional propagation algorithm using finite azimuthal aperture, *J. Acoust. Soc. Am.* **106** (1999) 3231–3239.
- [53] R. Doolittle, A. Tolstoy and M. Buckingham, Experimental bearing shifts as evidence of horizontal refraction in a wedge-like ocean, in *Progress in Underwater Acoustics*. H. M. Merklinger, ed. Plenum, New York, 1987, pp. 589–594.

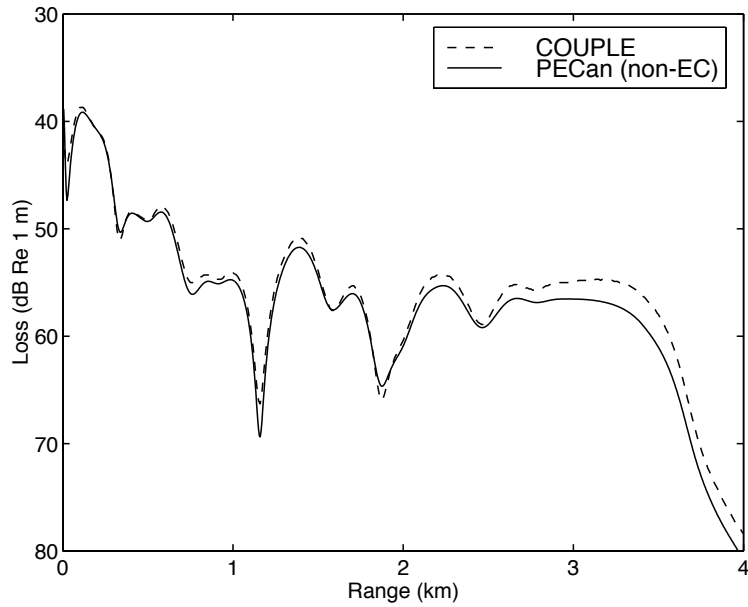


Figure 1: Transmission loss comparisons for the ASA wedge—PECan without energy conservation (non-EC). The source depth is 100 m and the receiver depth is 30 m.

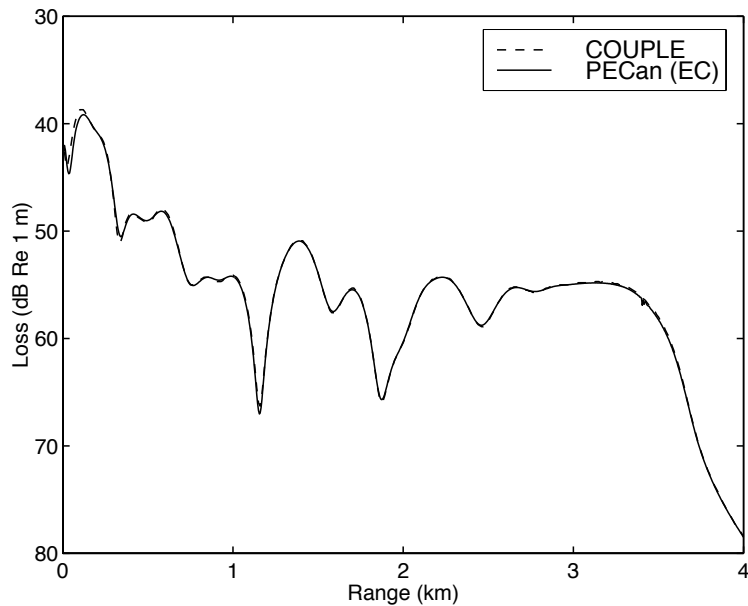


Figure 2: Transmission loss comparisons for the ASA wedge—PECan with energy conservation (EC). The source depth is 100 m and the receiver depth is 30 m.

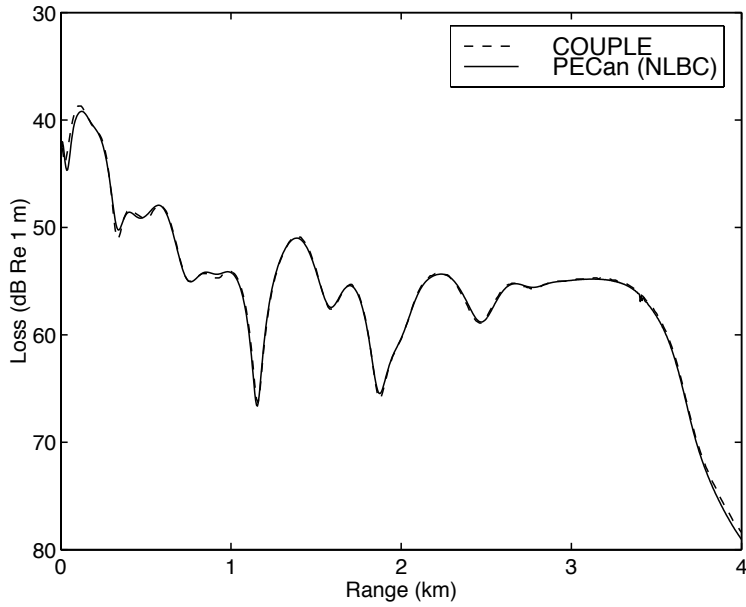


Figure 3: Transmission loss comparisons for the ASA wedge—PECan (EC) with nonlocal boundary condition (NLBC) at  $z = 250$  m. The source depth is 100 m and the receiver depth is 30 m.

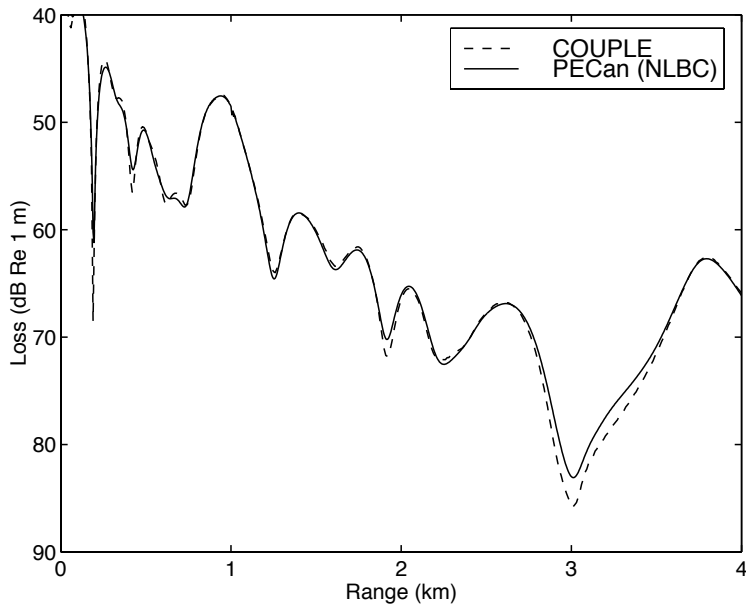


Figure 4: Transmission loss comparisons for the ASA wedge—PECan (EC) with nonlocal boundary condition (NLBC) at  $z = 250$  m. The source depth is 100 m and the receiver depth is 150 m.

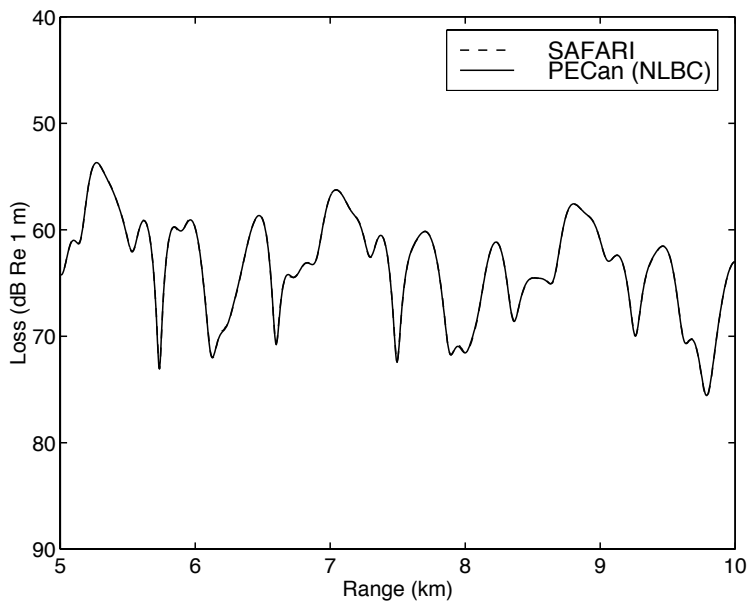


Figure 5: Transmission loss comparisons for the flat-surface Pekeris waveguide—PECan with nonlocal boundary condition (NLBC) at  $z = 100$  m. The source and receiver depths are 50 m.

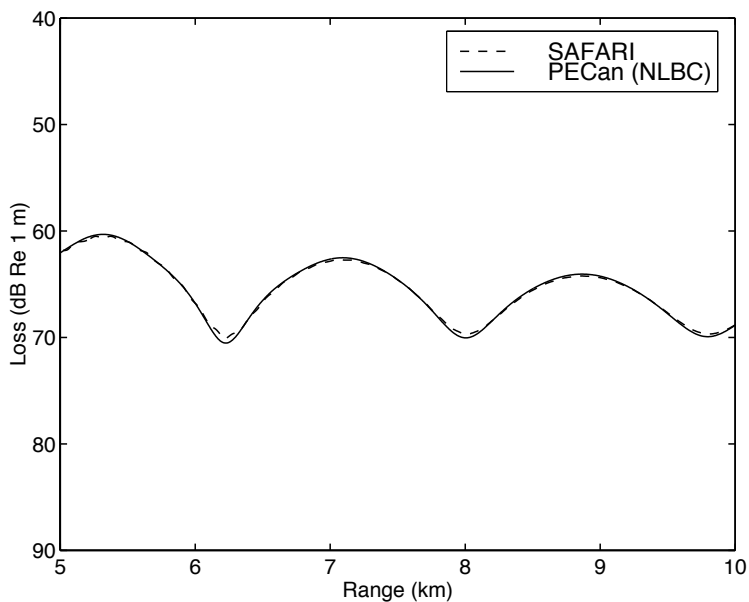


Figure 6: Transmission loss comparisons for the rough-surface Pekeris waveguide—PECan with nonlocal boundary conditions (NLBC's) at both  $z = 0$  m and  $z = 100$ . The source and receiver depths are 50 m.

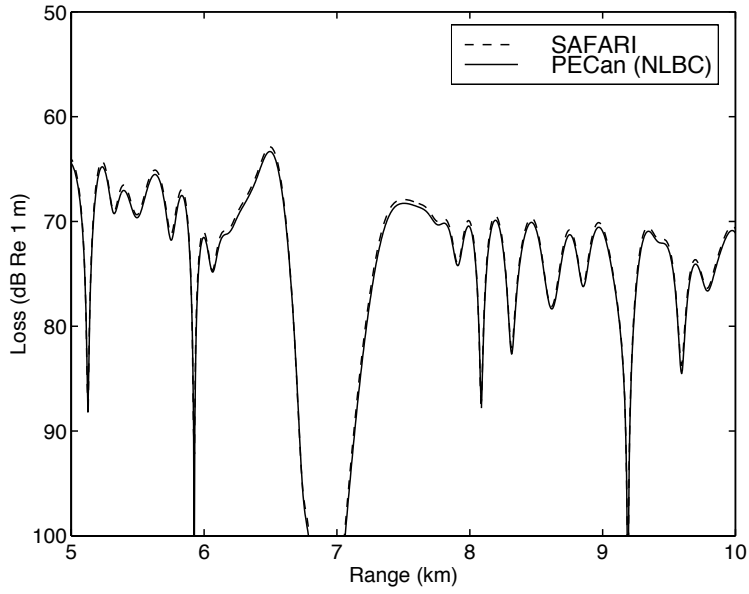


Figure 7: Transmission loss comparisons for the fluid-bottom Pekeris waveguide—PECan with nonlocal boundary condition (NLBC) at  $z = 110$  m. The source and receiver depths are 99.5 m.

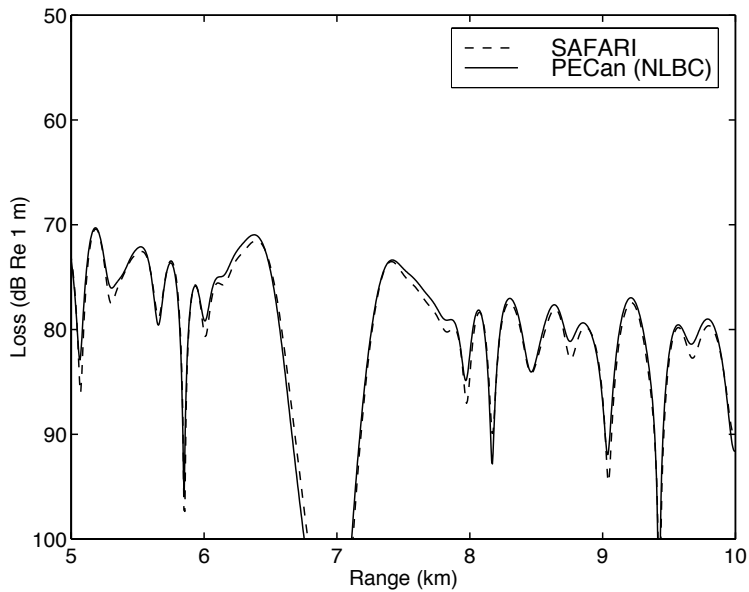


Figure 8: Transmission loss comparisons for the solid-bottom Pekeris waveguide—PECan with nonlocal boundary condition (NLBC) at  $z = 110$  m. The source and receiver depths are 99.5 m.

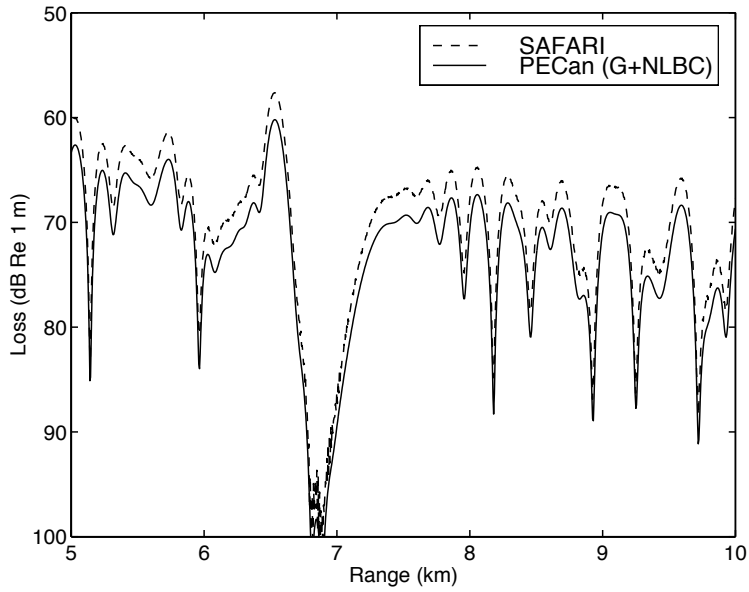


Figure 9: Transmission loss comparisons for the modified Pekeris waveguide—PECan with nonlocal boundary condition (NLBC) at  $z = 110$  m and using Greene's (G) source field. The source and receiver depths are 100 m.

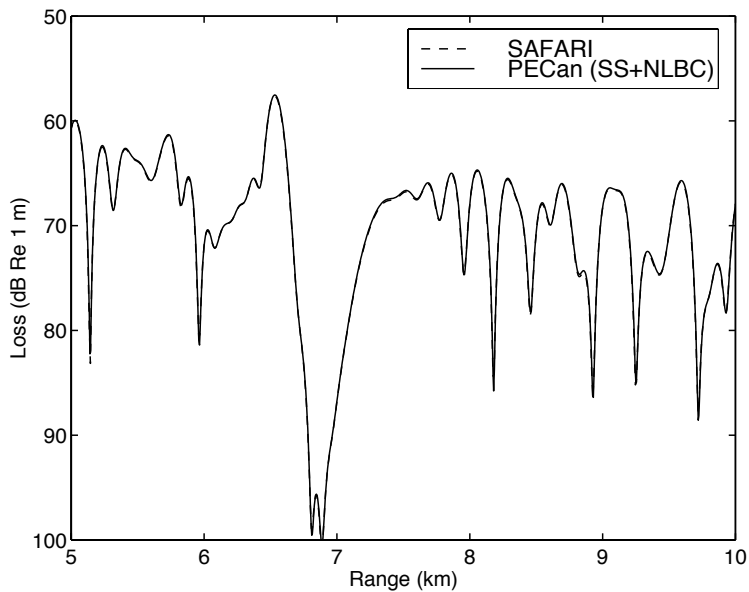


Figure 10: Transmission loss comparisons for the modified Pekeris waveguide—PECan with nonlocal boundary condition (NLBC) at  $z = 110$  m and using the self-starter (SS) source field. The source and receiver depths are 100 m.

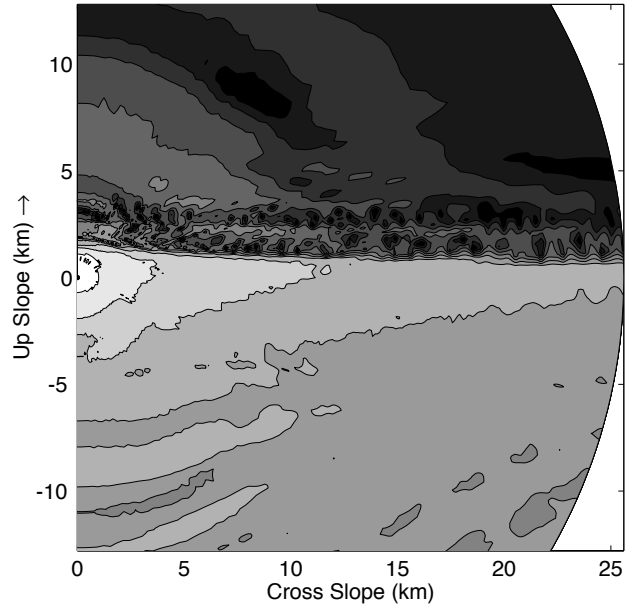


Figure 11:  $N \times 2D$  transmission losses for the Fawcett penetrable wedge for mode 3 excitation. The receiver depth is 36 m.

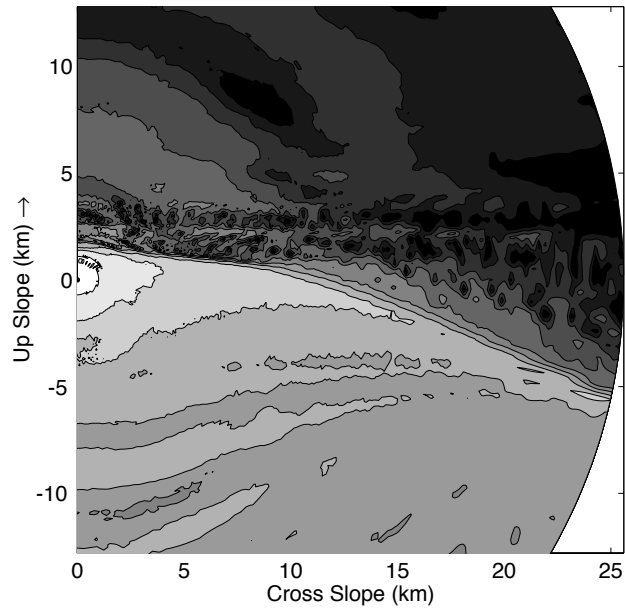


Figure 12: 3D transmission losses for the Fawcett penetrable wedge for mode 3 excitation. The receiver depth is 36 m.

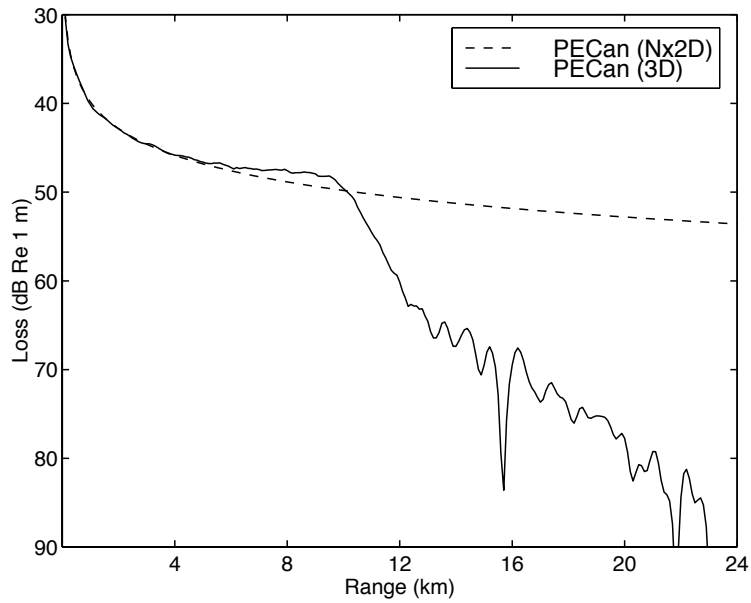


Figure 13: Transmission loss comparisons for the Fawcett penetrable wedge for  $\varphi = 90^\circ$  (cross-slope) and mode 3 excitation. The receiver depth is 36 m.

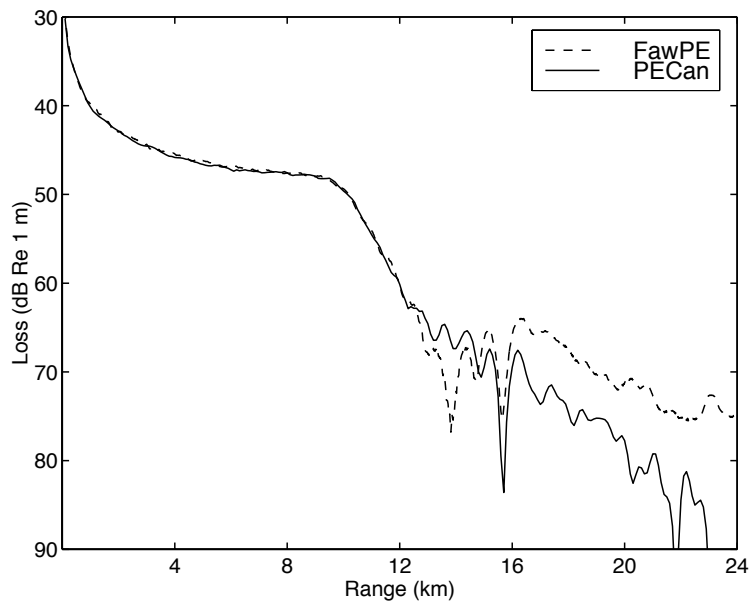


Figure 14: Transmission loss comparisons for the Fawcett penetrable wedge for  $\varphi = 90^\circ$  (cross-slope) and mode 3 excitation. The receiver depth is 36 m.

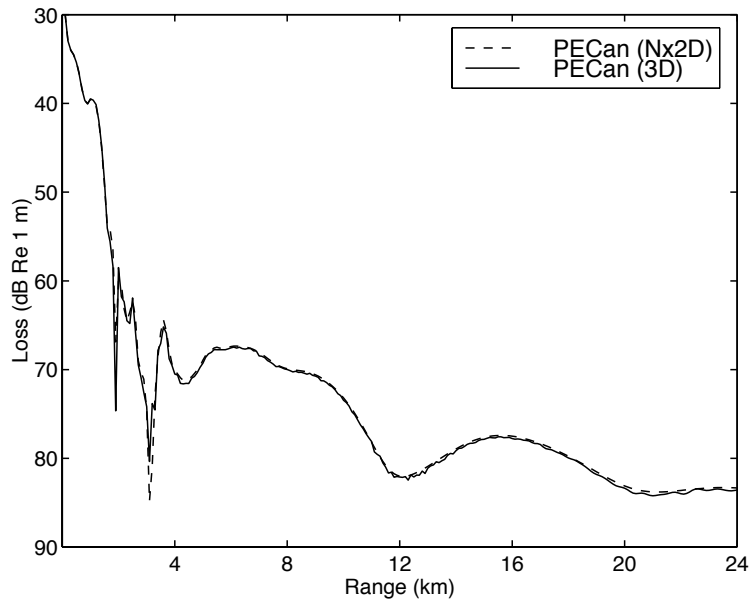


Figure 15: Transmission loss comparisons for the Fawcett penetrable wedge for  $\varphi = 0^\circ$  (upslope) and mode 3 excitation. The receiver depth is 36 m.

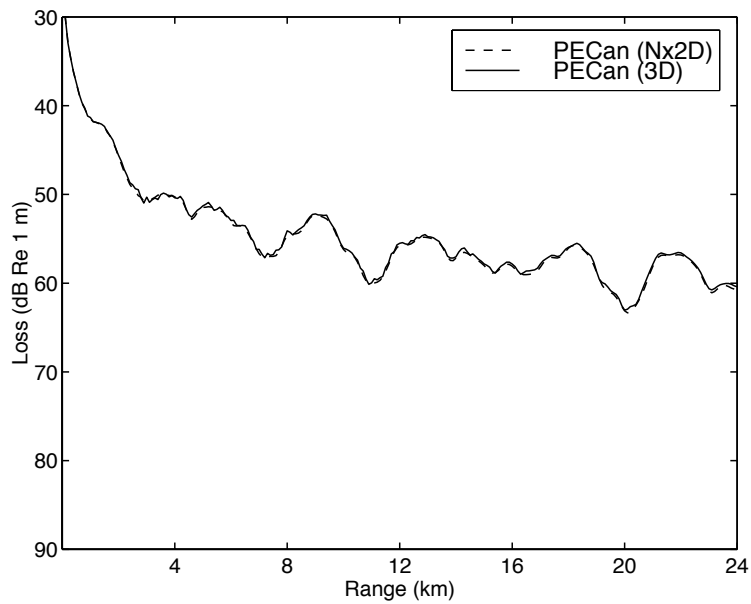


Figure 16: Transmission loss comparisons for the Fawcett penetrable wedge for  $\varphi = 180^\circ$  (downslope) and mode 3 excitation. The receiver depth is 36 m.

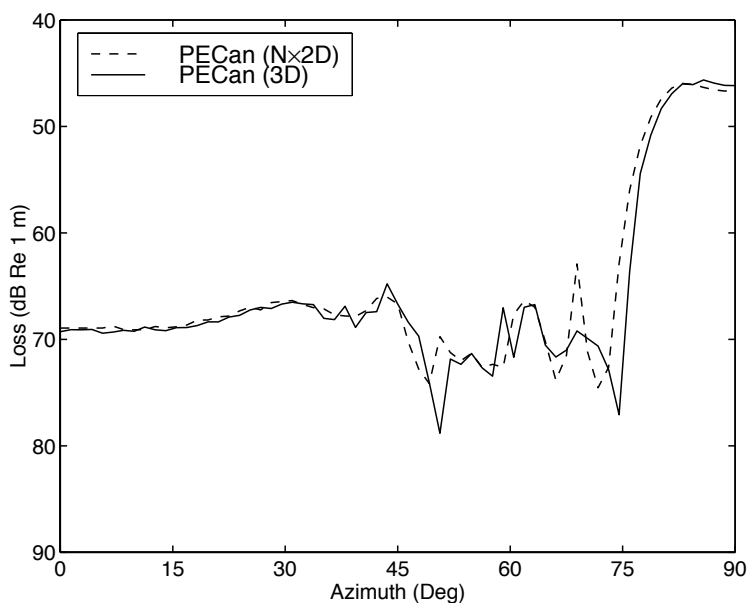


Figure 17: Transmission loss comparison along  $r = 5$ -km arc for the Fawcett penetrable wedge. The receiver depth is 36 m.

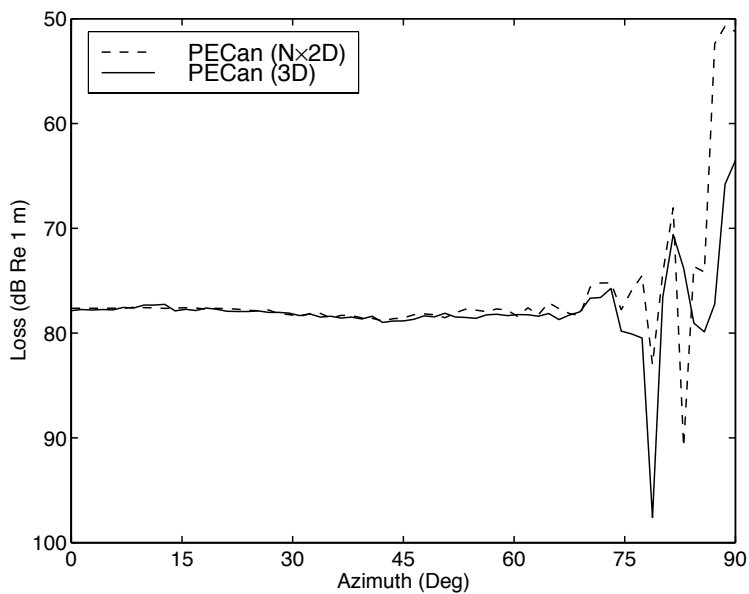


Figure 18: Transmission loss comparison along  $r = 15$ -km arc for the Fawcett penetrable wedge. The receiver depth is 36 m.

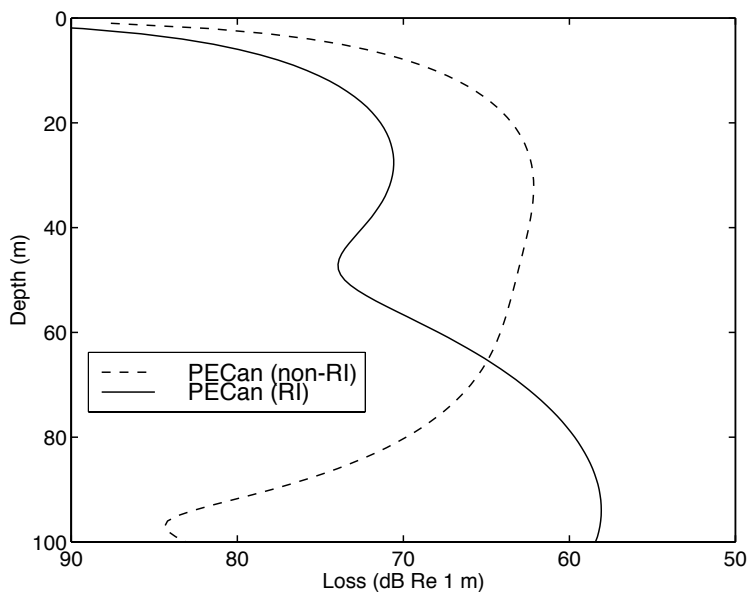


Figure 19: Range interpolated (RI) and non-RI transmission losses for SWAM Test Case 1a at a range of 15 km. The source depth is 30 m.

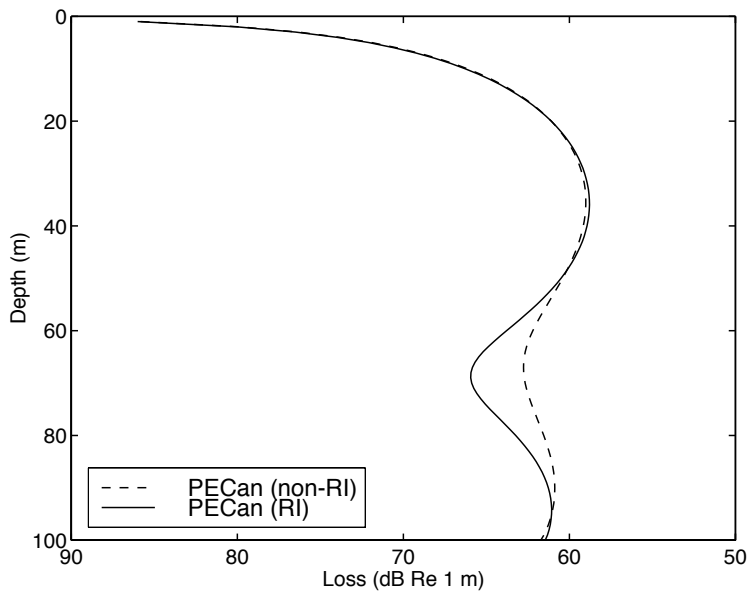


Figure 20: Range interpolated (RI) and non-RI transmission losses for SWAM Test Case 1c at a range of 15 km. The source depth is 30 m.

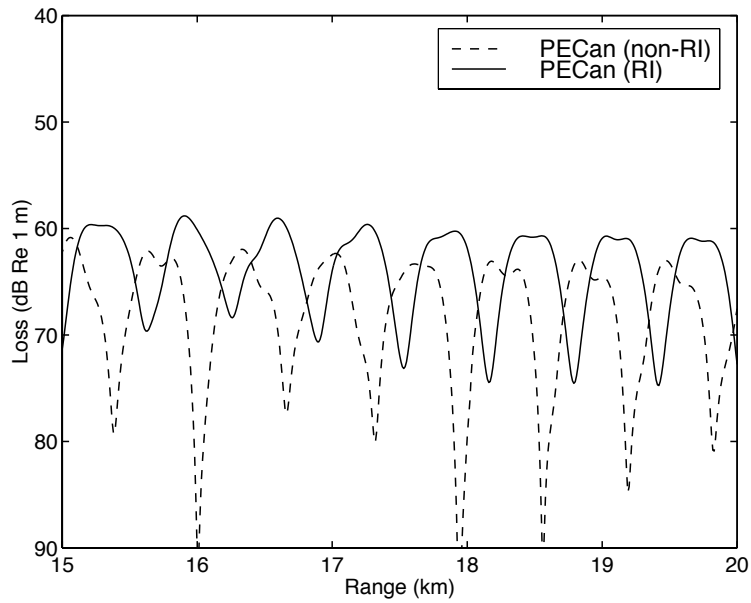


Figure 21: Range interpolated (RI) and non-RI transmission losses for SWAM Test Case 1a. The source depth is 30 m and the receiver depth is 35 m.

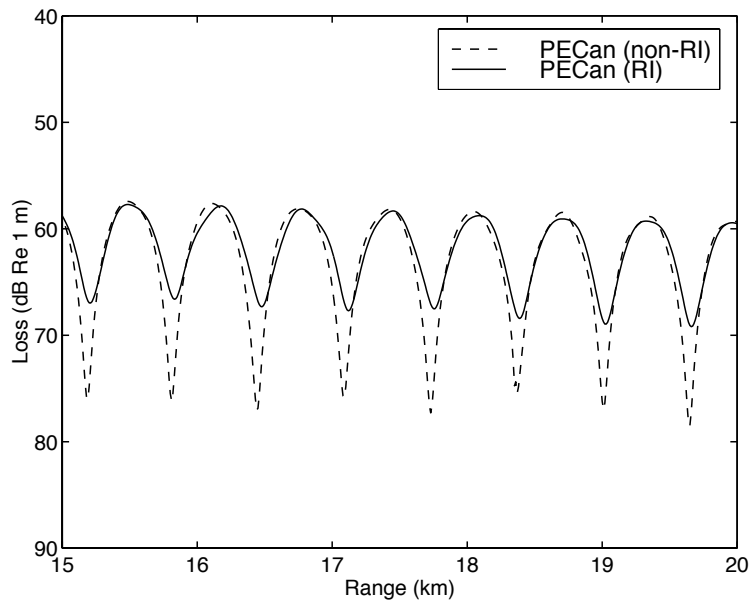


Figure 22: Range interpolated (RI) and non-RI transmission losses for SWAM Test Case 1c. The source depth is 30 m and the receiver depth is 35 m.

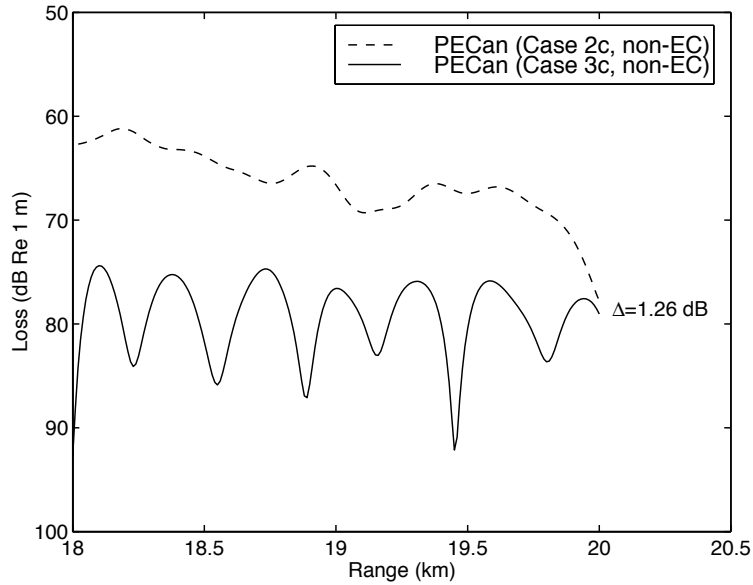


Figure 23: Reciprocal (non-RI, non-EC) transmission loss comparison for SWAM Test Cases 2c and 3c. The source/receiver depth combination is 30/35 m.

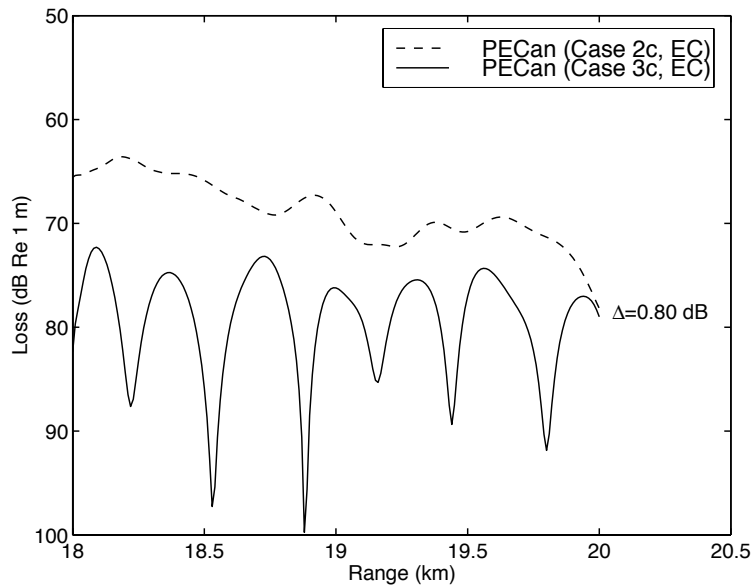


Figure 24: Reciprocal (non-RI, EC) transmission loss comparison for SWAM Test Cases 2c and 3c. The source/receiver depth combination is 30/35 m.

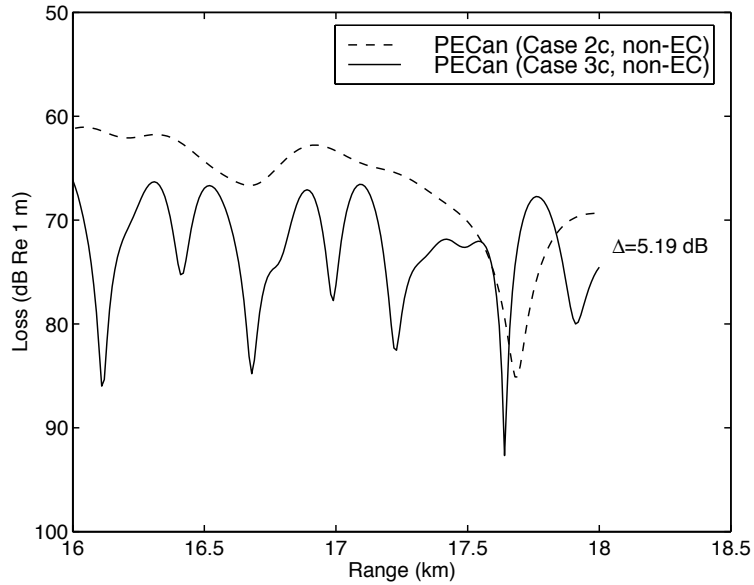


Figure 25: Reciprocal (RI, non-EC) transmission loss comparison for SWAM Test Cases 2c and 3c. The source/receiver depth combination is 30/35 m.

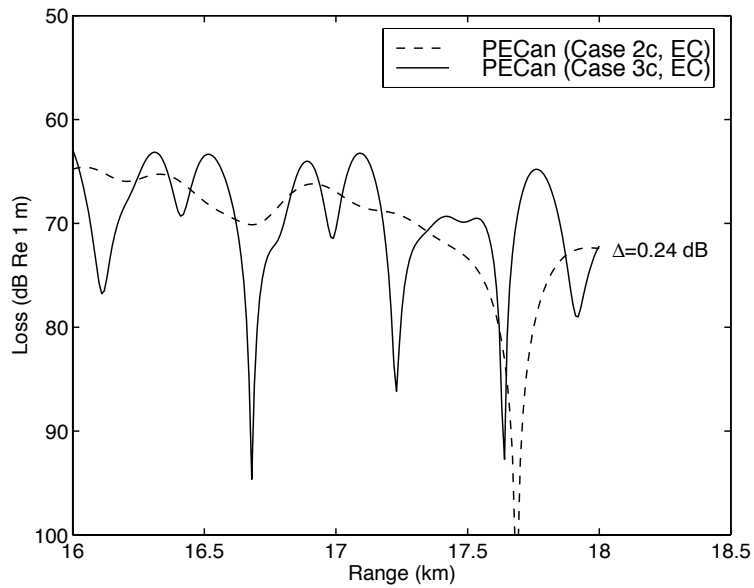


Figure 26: Reciprocal (RI, EC) transmission loss comparison for SWAM Test Cases 2c and 3c. The source/receiver depth combination is 30/35 m.

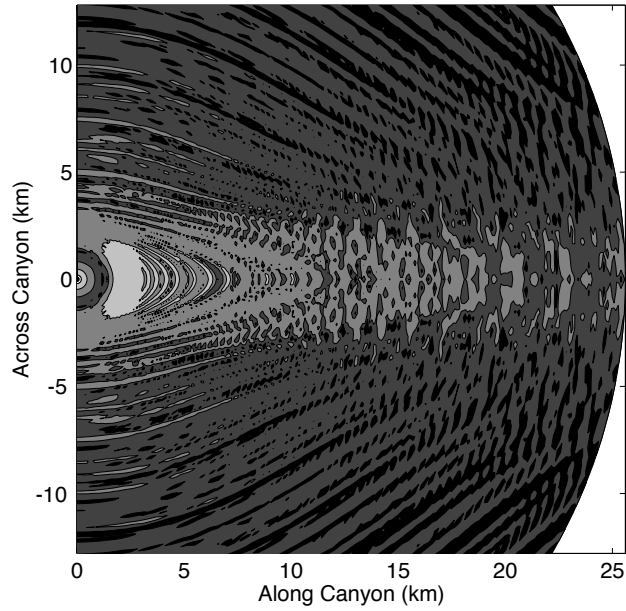


Figure 27:  $N \times 2D$  transmission losses for SWAM Test Case 4b (Synthetic Canyon). The source depth is 30 m and the receiver depth is 35 m.

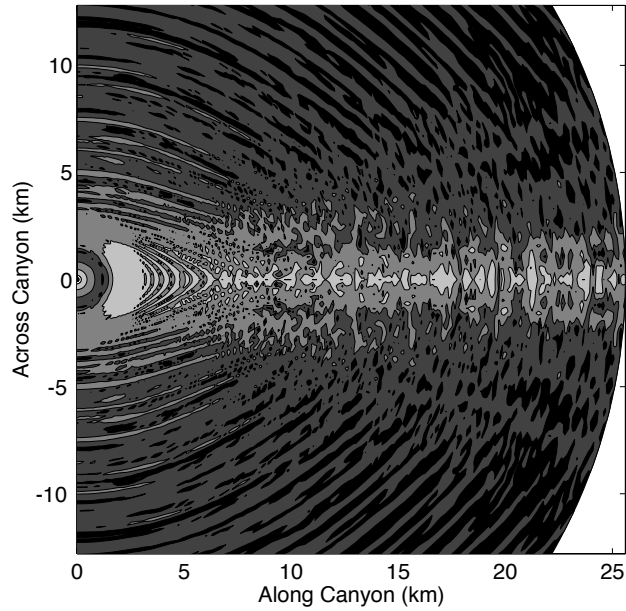


Figure 28: 3D transmission losses for SWAM Test Case 4b (Synthetic Canyon). The source depth is 30 m and the receiver depth is 35 m.

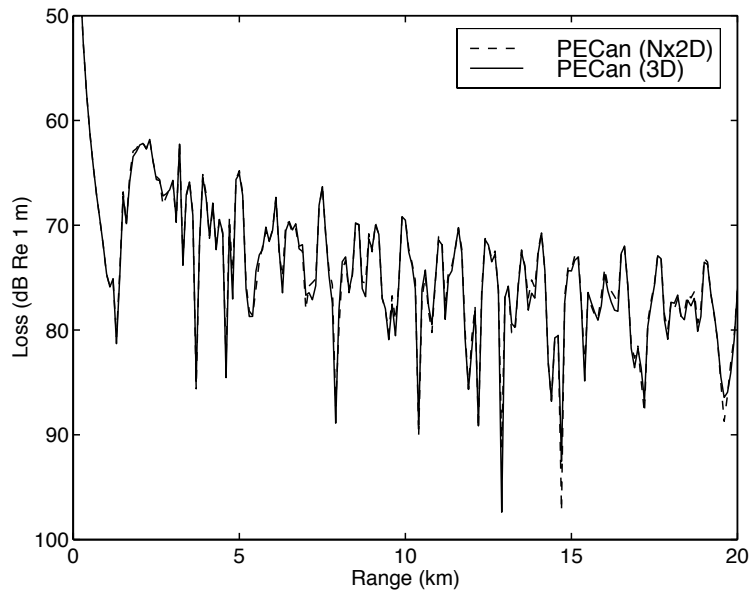


Figure 29: Transmission loss comparison across the channel axis ( $\varphi = 0^\circ$ ) for SWAM Test Case 4b. The source depth is 30 m and the receiver depth is 35 m.

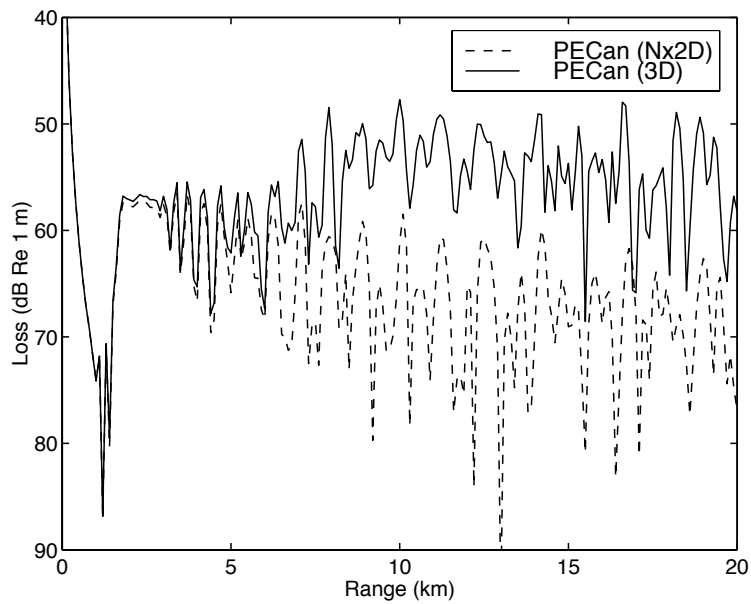


Figure 30: Transmission loss comparison along the channel axis ( $\varphi = 90^\circ$ ) for SWAM Test Case 4b. The source depth is 30 m and the receiver depth is 35 m.

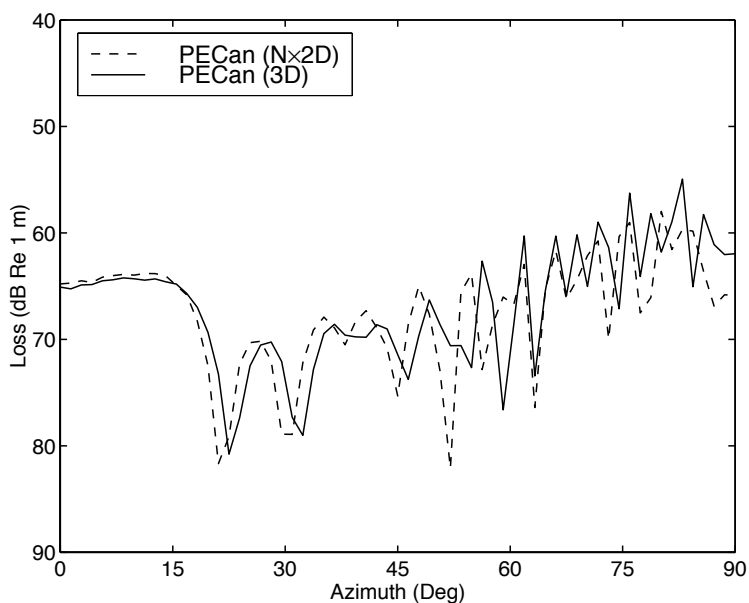


Figure 31: Transmission loss comparison along the  $r = 5$ -km arc for SWAM Test Case 4b. The source depth is 30 m and the receiver depth is 35 m.

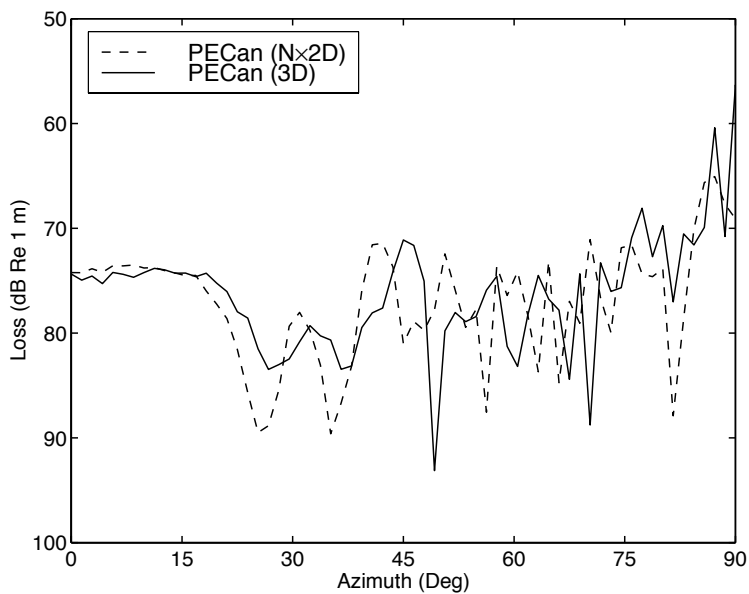


Figure 32: Transmission loss comparison along the  $r = 15$ -km arc for SWAM Test Case 4b. The source depth is 30 m and the receiver depth is 35 m.